HHS Public Access

Author manuscript

J Neurosci Methods. Author manuscript; available in PMC 2022 April 01.

Published in final edited form as:

J Neurosci Methods. 2021 April 01; 353: 109093. doi:10.1016/j.jneumeth.2021.109093.

Quantifying Mitochondrial Volume Density in Phrenic Motor Neurons

Matthew J. Fogarty[1,3,*], **Sabhya Rana**[1,*], **Carlos B. Mantilla**[1,2], **Gary C. Sieck**[1,2,#]

[1]Department of Physiology & Biomedical Engineering, Mayo Clinic, Rochester, MN 55905.

[2]Department of Anesthesiology and Perioperative Medicine, Mayo Clinic, Rochester, MN 55905.

[3]School of Biomedical Sciences, The University of Queensland, St Lucia, QLD, 4067, Australia.

Abstract

Background: Previous assessments of mitochondrial volume density within motor neurons used electron microscopy (EM) to image mitochondria. However, adequate identification and sampling of motor neurons within a particular motor neuron pool is largely precluded using EM. Here, we present an alternative method for determining mitochondrial volume density in identified motor neurons within the phrenic motor neuron (PhMN) pool, with greatly increased sampling.

New Method: This novel method for assessing mitochondrial volume density in PhMNs uses a combination of intrapleural injection of Alexa 488-conjugated cholera toxin B (CTB) to retrogradely label PhMNs, followed by intrathecal application of MitoTracker Red to label mitochondria. This technique was validated by comparison to 3D EM determination of mitochondrial volume density as a "gold standard".

Results: A mean mitochondrial volume density of ~11% was observed across PhMNs using the new MitoTracker Red method. This compared favourably with mitochondrial volume density (~11%) measurements using EM.

Comparison with Existing Method: The range, mean and variance of mitochondrial volume density estimates in PhMNs were not different between EM and fluorescent imaging techniques.

Conclusions: Fluorescent imaging may be used to estimate mitochondrial volume density in a large sample of motor neurons, with results similar to EM, although EM did distinguish finer mitochondrion morphology compared to MitoTracker fluorescence. Compared to EM methods,

[#]Correspondence: Gary C. Sieck, PhD, Vernon F. and Earline D. Dale Professor , Department of Physiology & Biomedical Engineering, Mayo Clinic, 200 1st St SW, Rochester, MN 55905, Phone: (507) 284 6850, sieck.gary@mayo.edu.

[*]Authors contributed equally to this study

CRediT Author Statement: Matthew Fogarty: Conceptualisation, Methodology, Validation, Investigation, Formal Analysis, Data Curation, Writing – Original draft, Writing – Review & Editing, Visualisation and Funding Acquisition. Sabhya Rana: Methodology, Validation, Investigation, Formal Analysis, Data Curation, Writing – Review & Editing and Visualisation. Carlos Mantilla: Conceptualisation, Methodology, Formal Analysis, Data Curation, Writing – Review & Editing, Resources, Supervision, Project Administration and Funding Acquisition. Gary Sieck: Conceptualisation, Methodology, Formal Analysis, Data Curation, Writing – Review & Editing, Resources, Supervision, Project Administration and Funding Acquisition.

Disclosure of Conflicts of Interest: None of the authors has any conflicts of interest, real nor perceived, to disclose.

the assessment of a larger sample size and unambiguous identification of motor neurons belonging to a specific motor neuron pool represent major advantages over previous methods.

Keywords

motor neuron; mitochondria; electron microscopy; confocal microscopy

1. INTRODUCTION

Mitochondria are essential for a variety of neuronal processes, ranging from energy production to cytosolic Ca^{2+} regulation to axonal and dendritic transport and the release and reuptake of neurotransmitters at synapses. Mitochondrial dysfunction is implicated in the etiology of a number of chronic diseases including neurodegenerative diseases such as amyotrophic lateral sclerosis (ALS), Parkinson's and Alzheimer's disease (Dupuis et al., 2004; Hauser and Hastings, 2013; Hirai et al., 2001). Changes in mitochondrial morphology are commonly observed in motor neurons of ALS patients as well as rodent models of ALS (Bendotti et al., 2001; Martin et al., 2007; Sasaki et al., 2004; Sasaki and Iwata, 2007; Wong et al., 1995).

Past measurements of mitochondrial morphology have contributed to our understanding of the role of mitochondrial dysfunction plays in a variety of motor neuron pathologies. However, the overwhelming majority of previous studies examining motor neuron mitochondrial morphology have used *in vitro* methods, either cultured motor neuron-like cells, embryonic motor neurons or induced pluripotent stem cells. Importantly, these approaches may not reflect the normal physiological ATP demand of motor neurons *in situ*. Additionally, the media in which *in vitro* preparations are maintained may influence metabolism (Vande Voorde et al., 2019). As such, the *in vivo* neurobiology of mitochondria in motor neurons remains poorly described, with observations of mitochondrial morphology of motor neurons *in situ* predominated by electron microscopy (EM), with limited sample size, little attempt at quantification and an inability to disambiguate discrete motor pools (Deng et al., 2006; Hart et al., 1977; Hirano et al., 1984a; Hirano et al., 1984b; Jaarsma et al., 2000; Kong and Xu, 1998).

Inarguably, EM offers a superior nano-scale resolution of individual mitochondrion, albeit at the expense of markedly limited sample sizes. However, recent fluorescent deconvolution techniques are able to accurately quantify a variety of sub-cellular structures in motor neurons, including synaptic inputs (Fogarty et al., 2013a; Rana et al., 2019a), dendritic arbours (Fogarty et al., 2016a; Fogarty et al., 2017a; Kanjhan et al., 2016) and axonal projections (Kanjhan et al., 2016). Additionally, these approaches allow use of fluorescent labeling to disambiguate motor neuron pools innervating specific muscles (Brandenburg et al., 2018; Brandenburg et al., 2020; Fogarty et al., 2018b; Ishihara et al., 1995; Ishihara et al., 2001; Mantilla et al., 2009; Prakash et al., 1993).

Phrenic motor neurons innervate the diaphragm muscle (DIAm), which is responsible for essential ventilatory and expulsive motor behaviors required for the survival of mammals (Fogarty et al., 2018a; Fogarty and Sieck, 2019b; Herxheimer, 1949; Sieck and Fournier, 1989; Sieck, 1991). Phrenic motor neurons reside in the ventral horn of the cervical spinal

cord (segments C_{3-5}) in rats (Fogarty et al., 2018b; Prakash et al., 1994; Rana et al., 2017; Song et al., 2000) and between C_{3-6} in other mammalian species (Fogarty and Sieck, 2019b). In DIAm muscle fibers, mitochondrial volume densities range from ~1-25%, depending on fiber-type (Sieck et al., 1998). It is likely that this range of mitochondrial volumes is mirrored within their innervating phrenic motor neurons, due to the matching of discharge and activation/fatigue properties of motor units (Mantilla and Sieck, 2011; Sieck and Fournier, 1989; Sieck, 1991).

The aim of the present study was to develop and validate a three-dimensional confocal microscopy-based method to determine mitochondrial volume density using MitoTracker Red fluorescent labeling in retrogradely identified phrenic motor neurons. We hypothesize that the mitochondrial volume density in phrenic motor neurons determined using our MitoTracker fluorescence method is similar to that determined by EM in putative phrenic motor neurons located in C_3-C_5 ventral spinal cord.

2. MATERIALS AND METHODS

2.1 Ethical approval

All procedures were conducted in accordance with the American Physiological Society's Animal Care Guidelines, the National Institutes of Health guide for the care and use of laboratory animals (NIH Publications #8023, revised 1978) and were approved by the Institutional Animal Care and Use Committee at Mayo Clinic (Protocol #A00003068-17).

2.2 Experimental animals

We used 10 pathogen-free 6-months old Fisher 344 rats (5 males and 5 females), obtained from Charles River Laboratories. Although sex as a biological variable cannot be excluded, we previously observed no difference between males and females in the number, size and distribution of phrenic motor neurons (Brandenburg et al., 2020; Fogarty et al., 2018b), or in DIAm motor unit properties (Brandenburg et al., 2020; Fogarty et al., 2019a; Fogarty et al., 2019b; Gonzalez Porras et al., 2019), including those that directly relate to oxygen consumption and ATP requirements (Fogarty et al., 2020a). Animals were maintained on an alternating 12:12 h light-dark cycle with *ad libitum* access to fresh water and rat chow. An acclimation period of at least 48 h was provided before conducting any experimental procedures.

2.3 Phrenic motor neuron labeling

In 6 rats (3 males and 3 females) destined for fluorescent MitoTracker assessment of mitochondria and 2 rats (1 of either sex) destined for EM studies we performed bilateral intrapleural injection of CTB (10 μl 0.2% Alexa 488-conjugated CTB), in a manner identical to previous studies (Alvarez-Argote et al., 2016; Gransee et al., 2013, 2015; Mantilla et al., 2009; Mantilla et al., 2013; Mantilla et al., 2018; Rana et al., 2017; Rana et al., 2020). After three days, this intrapleural injection technique completely labels phrenic motor neurons via retrograde transport (Fogarty et al., 2018b; Mantilla et al., 2009; Rana et al., 2019b).

2.4 Intrathecal MitoTracker Red delivery, tissue collection and processing

Three days after labeling phrenic motor neurons, rats were deeply anaesthetised with intraperitoneal injection of ketamine (80 mg/kg) and xylazine (20 mg/kg). To access the subarachnoid space of the spinal cord, a bilateral dorsal laminectomy was performed at C_3 followed by opening the dura, in a manner adapted from previous studies (Gransee et al., 2015; Mantilla et al., 2013). Thereafter, a solution of MitoTracker Red (M7512, Molecular Probes, Eugene, OR) diluted in saline (6 μl per 1 ml of saline, 300 nM) (Delmotte et al., 2017; Delmotte et al., 2020) was steadily infused onto the spinal cord (~10 μl of MitoTracker Red solution every 10 min) over a 90-min period. The concentration of MitoTracker Red used to label mitochondria in phrenic motor neurons was consistent with that used in previous studies on a variety of cell types (Aravamudan et al., 2014; Aravamudan et al., 2017; Delmotte et al., 2017; Ryan et al., 2015).

Immediately following labeling mitochondria, rats were perfused intracardially with a 0.1 M phosphate buffered saline (PBS), euthanized via exsanguination and then perfused with 4% paraformaldehyde in 0.1 M PBS. The C_1-C_6 segment of the spinal cord was then dissected, post-fixed in 4% paraformaldehyde for 24 h, and then transferred to 25% sucrose in 0.1 M phosphate buffer for 3 days at 4°C. Spinal cord tissue embedded in cryomoulds (VWR, Radnor, PA), was cut in longitudinal horizontal sections at 70 μm and mounted on Tissue Tack slides (Polysciences, Warrington, PA) that were pre-coated with Cell-Tak adhesive (Becton Dickinson Lab Ware, Bedford, MA). Cut sections were then mounted in prolong gold anti fade media (Cat# P36934, ThermoFisher, Weltham, Ma), cover-slipped and stored until imaging, within 3 weeks of processing, in a manner consistent with past reports (Brandenburg et al., 2018; Brandenburg et al., 2020; Fogarty et al., 2018b; Rana et al., 2017; Rana et al., 2019a; Rana et al., 2020).

2.5 Confocal Imaging

Labeled phrenic motor neurons in the cervical spinal cord sections were visualized with an Olympus FV2000 laser confocal microscope (Olympus Life Sciences Solutions, Waltham, MA) equipped with argon (488 nm) and green HeNe (543 nm) lasers. Three-dimensional confocal imaging techniques have been previously reported in detail (Fogarty et al., 2018b; Issa et al., 2010; Mantilla et al., 2018; Prakash et al., 1993, 1994; Prakash et al., 2000; Sieck et al., 1999; Zhan et al., 2000). Briefly, all images were acquired at 12-bit resolution in an array of 1024x1024 pixels using a 60x Plan Apo oil-immersion objective (NA 1.40, WD 0.15 mm) with a step size of 0.5 μm (voxel dimensions: 0.207 x 0.207 x 0.5 μm). In order to achieve the systematic randomised sampling necessary for our stereological approach, the mosaic imaging feature was used. This allowed for the ready identification of rostral and caudal portion of a cervical spinal cord section and ensured that there were no gaps or bias in the location of our samples within the phrenic motor pools. Sequential two-channel imaging was performed using a dichroic mirror beam splitter that allows transmission of 555-615 nm (reflects 480-555 and 615-800 nm) and appropriate band pass emission filters (495-535 nm and 575-630 nm - for Alexa 488 and MitoTracker Red, respectively). Since image analysis is highly dependent on image quality, several steps were taken to ensure images were of optimal quality. To reduce cross-talk, laser illumination was done sequentially for the imaging of each optical slice. The empirically-calculated point spread

function for the 60x objective was used to set the step size, as previously reported (Prakash et al., 1993, 1994; Sieck et al., 1999). Laser intensity and photomultiplier settings were adjusted to maintain black level of the blank sections (no primary antibody) to less than 10% of the dynamic range and to prevent saturation.

2.6 Fluorescent mitochondrial density analysis in phrenic motor neuron somas

Following the acquisition of confocal mosaic *z*-stacks, individual regions of interest were selected comprising an identified phrenic motor neuron within our sampling scheme and the portion of the *z*-stack in which the soma was contained. These individual phrenic motor neuron regions of interest were saved in tiff format and then further processed for mitochondrial volume density. Following the selection of a region of interest, the *z*-stack was deconvolved using module in the NIS-Elements AR software package (Nikon). A blind deconvolution algorithm (Point Scan Confocal, 3 iterations, which gave the inverse of the point spread function) was used in which the most probable combination of point spread function was estimated for the given image, thus obviating the need to obtain a point spread function for the optical system for each image acquisition session. Following deconvolution, the 3D object measurement plugin in the NIS-Elements AR software package was utilized to binarize and threshold the image stack. Briefly, an intensity threshold was used such that by lowering the threshold, more pixels were considered to be true signal and by raising the threshold, less pixels were considered to be part of the true (above background signal). This thresholding was done by visualizing the image histogram in conjunction with visualizing the MitoTracker red fluorescence signal at a mid-nuclear section of the region of interest. When the discrete puncta were all included within the threshold (by pseudo-colouring with fuchsia), the image was binarized. Subsequently, the plugin allowed identification of individual mitochondrial objects within the phrenic motor neuron, with binarized pixel areas that overlapped in the *z*-axis considered to be part of a continuous volume (mitochondrial element). Detailed morphometric analysis of all mitochondrial elements was obtained. Mitochondrial volume density was established for an individual phrenic motor neuron by aggregating the summed volume of all mitochondrial elements detected on the deconvolved red (MitoTracker Red) channel, divided by the phrenic motor neuron volume, measured using surface/volume creation in elements, in a manner identical to past reports (Rana et al., 2019b; Rana et al., 2020). Similar to the method described above, thresholding (accomplished by visualizing the image histogram in conjunction with the CTB fluorescence signal at a mid-nuclear section) was used to distinguish the extent of the soma. Finally, the somal volume created from overlapping binarized pixels in the *z*-axis.

Images were converted to 8-bit in NIS Elements for presentation only. No thresholding or post-imaging processing was applied for any image. Each channel was pseudo-colored in Adobe Photoshop by changing the color gamut (RGB). Only brightness and contrast levels were adjusted linearly if needed to facilitate presentation of multiple colors.

2.7 Fluorescent mitochondrial density analysis in phrenic motor neuron dendrites

For sampling primary and secondary phrenic motor neuron dendrites, three relatively isolated motor neurons were selected from each rat where primary and secondary dendrites could be unambiguously identified as belonging to a particular motor neuron soma. The

mitochondrial volume density of primary and secondary dendrites was assessed in a manner identical to that of motor neuron somas. Following deconvolution, mitochondrial elements were created within the bounds of the CTB-labeled phrenic motor neuron dendrites. Mitochondrial volume density was established for an individual phrenic motor neuron by aggregating the summed volume of all mitochondrial elements detected on the deconvolved red (MitoTracker Red) channel, divided by the volume of dendrite being assessed. The volume of the dendritic compartment was derived from the formula for a cylinder, with the length and diameter measured within the elements software in a manner identical to past reports for dendrites (Fogarty et al., 2013a; Klenowski et al., 2015; Rana et al., 2020).

2.8 Electron microscopy tissue collection, processing and serial block face imaging

Mitochondrial volume density in phrenic motor neurons was assessed in a separate cohort of 4 rats (2 female, 2 male) anesthetised via an intraperitoneal injection of ketamine (80 mg/kg) and xylazine (20 mg/kg). The dissection process started 1 h after the onset of anaesthesia to approximate the time of anaesthesia exposure in rats undergoing the MitoTracker procedure (time control). Subsequently, while under anaesthesia, the cervical spinal (C_1-C_6) cord was freshly dissected from the vertebral column and carefully placed in a dissection dish filled with 0.1 M phosphate buffer solution (PBS). Under a dissection microscope, the cervical spinal cord was bisected in the sagittal plane into left and right halves, and the dorsal horn of the spinal cord was removed, followed by the dissection of the C_3, C_4 and C_5 areas of the ventral horn. These spinal cord segments were placed in Trump's fixative (1% glutaraldehyde and 4% formaldehyde in 0.1 M PBS, pH 7.2). These segments were then rinsed in 0.1 M PBS (pH 7.2), followed by 30 min postfix in phosphate-buffered 1% osmium tetroxide (OsO_4). The entire procedure including anaesthesia and dissection was completed within ~30 min comparable to the time taken for anaesthesia and perfusion in the MitoTracker procedure. After rinsing in distilled water, segments were shaved down to fit the block-face EM chuck (~0.5 mm^3), stained with 2% uranyl acetate for 15 min at 60°C, rinsed, dehydrated in progressively higher concentrations of ethanol and 100% propylene oxide, and embedded in Spurr's resin. Semi-thin survey sections (200 nm) were used to find areas of the blockface that contained putative phrenic motor neurons

2.9 Electron microscopy mitochondrial density analysis

Serial blockface EM was carried out on regions of interest determined from semi-thin survey sections, with the distance between each serial image being 0.1 μm. Putative phrenic motor neurons were identified within each serial block face image by the presence of a large nucleolus, a large cytoplasm to nuclear ratio and a diameter of >15 μm. Within these images, mitochondria were readily identified, characterised by the presence of internal cristae and location within the neuronal cytoplasm. To sample the volume density of mitochondria within these samples, a Cavalieri volume estimation scheme was employed (Nyengaard and Gundersen, 2006; Prakash et al., 1994; Slomianka, 2020). Within these putative phrenic motor neurons, mitochondrial areas were manually traced, and their area, circularity, perimeters, and long- and short-axes recorded. Thereafter, the boundary of the motor neuron was traced and the area determined. At 2 μm intervals from this centre, Cavalieri *z*-slices were obtained in both directions. This process was then repeated for each putative phrenic motor neuron sampled. The mean area density of mitochondria were determined for each

Cavalieri *z*-slice, and a mitochondrial volume density was calculated based on the number of total slices assessed and the distance between each slice (2 μm), for each putative phrenic motor neuron.

2.10 Outcome measures

Our primary outcome measure was mitochondrial volume density, which was based on the sum of all mitochondrial volumes within a labeled phrenic motor neuron, or the sum of cavalieri mitochondrial volume estimates in putative phrenic motor neurons, in fluorescent and serial blockface EM material, respectively. There were three secondary outcome measures: i) mean mitochondrion volume – the volume of individual mitochondria within a particular motor neurons; ii) mitochondrial aspect ratio – the long axis divided by the short axis of an individual mitochondrion or mitochondrial volume element; and iii) mitochondrial sphericity or circularity - how closely a 3D mitochondrial element or a 2D cavalieri mitochondrion structure approximates a perfect sphere or circle, respectively. These morphological volumes (Arnold et al., 2011; Miller et al., 2016; Sieck et al., 1998) and shape factor estimates (Aravamudan et al., 2014; Arnold et al., 2011; Delmotte et al., 2017; Delmotte and Sieck, 2019; Koopman et al., 2005; Leduc-Gaudet et al., 2015; Picard et al., 2013; Ryan et al., 2018) have been previously described in detail.

2.11 Statistical Analysis

For fluorescent imaging of mitochondrial density, we sampled every 20th phrenic motor neuron in an unbiased stereological manner, starting from a random starting point (1-20) and commencing sampling with the most rostral phrenic motor neuron identified on the left side of the spinal cord designated #1, then proceeding to the phrenic motor neuron identified in the most caudal portion of the same side, before crossing to the right side of the spinal cord. We included only phrenic motor neurons whose entire volume was comprised within the *z*-stack. In addition, only phrenic motor neurons with intact somal bodies were considered for analysis. Previously, ~20-25 phrenic motor neurons per animal have been shown to robustly sample the full gamut of phrenic motor neuron sizes in rodents (Brandenburg et al., 2020; Fogarty et al., 2018b; Mantilla et al., 2018; Rana et al., 2019a; Rana et al., 2019b; Rana et al., 2020). Based on multiple morphological properties of adult rodent phrenic motor neurons (Brandenburg et al., 2020; Fogarty et al., 2018b; Rana et al., 2019a; Rana et al., 2019b; Rana et al., 2020), we did not expect to observe a sex difference, so data from males and females are collapsed into single groups.

We used Prism 8 for all data analysis (Graphpad, Carlsbad, CA). Each data set was assessed for normality with D'Agostino and Pearson tests. For comparisons between two groups, unpaired two-tailed Student's *t*-tests were used. For comparisons of distributions, Kolmogorov-Smirnov tests were used. In cases where comparisons of non-normally distributed data were undertaken, Mann-Whitney U-tests were used to compare group means. All data are reported as the mean ± 95% confidence interval of the mean, unless otherwise specified. Statistical significance was established at the $P<0.05$ level.

3. RESULTS

3.1 Labeling of phrenic motor neurons by intrapleural injection of CTB and identification of putative phrenic motor neurons in semi-thin survey sections

Phrenic motor neurons are readily identified following CTB labeling, and appear within a discrete pool in 70 μm horizontal sections of the ventral cervical spinal cord (Figure 1A). Note that these images contain a marked heterogeneity of phrenic motor neuron somal sizes, in agreement with past studies (Brandenburg et al., 2020; Fogarty et al., 2018b; Mantilla et al., 2018; Prakash et al., 2000; Rana et al., 2019a; Rana et al., 2019b; Rana et al., 2020). In EM images, putative phrenic motor neurons were identified in semi-thin survey sections by their large long and short axis diameters (>15 μm), the larger cytoplasm to nuclear ratio and the presence of a nucleolus (Figure 1B), in an identical manner used to distinguish motor neurons from other neuronal types in various ventral horn histological preparations (Banks et al., 2005; Campa and Engel, 1970; Fogarty et al., 2013b; Fogarty et al., 2015b; Fogarty et al., 2020b; Lance-Jones, 1982; Mitchelle and Watson, 2016; Oppenheim, 1986; Steyn et al., 2013).

3.2 Image processing of MitoTracker Red signal in phrenic motor neurons

A region of interest was created for *z*-stacks (0.5 μm *z*-step) comprising CTB-labeled phrenic motor neurons (Figure 2A) and the MitoTracker Red labeled mitochondria (Figure 2B). The unprocessed MitoTracker Red signal was readily observed at different depths in the *z*-stack (Figure 2C), and was predominantly found in the perinuclear cytoplasm. Binarization (the thresholding and edge delineation) of a CTB-labeled phrenic motor neuron and the 3D volume rendering is illustrated in Figure 2 panels D and E). Within each *z*-slice, the unprocessed MitoTracker Red signal (Figure 3A) was deconvolved in the *xy* plane (Figure 3B). Following deconvolution, the MitoTracker fluorescence was binarized. Thresholding was accomplished using visualization of the signal and image intensity histogram at a mid-nuclear *z*-slice, with care taken to ensure that discrete puncta were not missed, incidental background included nor obliteration of discrete structures (Figure 4). Based on the local contrast and binarization of each *z*-slice image of the deconvolved MitoTracker Red channel, a 3-dimensional volume was created using the volume-generating algorithm within the NIS Elements software package (Figure 3C and Figure 4C). Based on all thresholded areas (i.e., binarized signal) within a *z*-slice (Figure 5), volumes (voxel-based mitochondrial elements) were created, compiled automatically from pixel areas that overlap in the *z*-axis (Figure 3C and Figure 5). This reconstruction is similar to other volume reconstructions previously developed and validated for motor neurons, including phrenic motor neurons (Fogarty et al., 2013a; Issa et al., 2010; Rana et al., 2019a; Rana et al., 2019b; Rana et al., 2020). Each mitochondrial volume element had its volume, *x*-, *y*- and *z*-axes, surface area and sphericity determined. This process usually resulted in the generation of ~200-400 mitochondrial elements per phrenic motor neuron (Figure 3C, Figure 4C and Figure 5).

3.3 Analysis of serial blockface electron microscopy of mitochondria in putative phrenic motor neurons

Serial blockface EM was carried out on regions of interest determined from semi-thin survey sections, with the distance between each serial image being 0.1 μm. Putative phrenic motor neurons were identified within each serial block face image by the presence of a large nucleolus, a large cytoplasm to nuclear ratio and a diameter of >15 μm (Figures 6 and 7). Within these images, mitochondria were readily identified, characterised by the presence of internal cristae and location within the neuronal cytoplasm (Figure 7). Note that mitochondria exhibit an impressive array of morphological phenotypes (Figure 7B). Serial blockface EM images containing putative phrenic motor neurons comprised *z*-stacks containing ~80-250 *z*-slices (Figure 6). To sample the volume density of mitochondria within these samples, a Calvalieri volume estimation scheme was employed. For each ultrathin section of the putative phrenic motor neuron containing a prominent nucleolus and large cytoplasmic extent, mitochondrial areas were manually traced, with their area, circularity, perimeters, and long- and short-axes determined. Following this, the boundary of the motor neuron was traced and the area determined. At 2 μm intervals from the center, Cavalieri *z*-slices were obtained in both directions, and this process was then repeated. The mean area density of mitochondria was obtained for each Cavalieri *z*-slice and the volume density calculated based on the number of total slices assessed and the distance between each slice (2 μm).

3.4 Mitochondrial volume density measurements based on fluorescent and electron microscopic analysis techniques

An example of silhouetted mitochondrial volumes sampled using MitoTracker Red within labeled phrenic motor neurons exhibits the characteristic perinuclear location of mitochondria within neurons (Figure 8A). An example of silhouetted mitochondrial volumes sampled using serial blockface EM within putative phrenic motor neurons exhibited the characteristic perinuclear location of mitochondria within neurons (Figure 8B).

The mean mitochondrial volume density within motor neurons was equivalent when assessed using either technique. Using MitoTracker Red and confocal imaging, the mean mitochondrial volume density was 9.3 ± 1.0 % with a median of 8.0%. Using 3-dimensional EM, the mean mitochondrial volume density was 8.9 ± 2.6 % with a median of 8.6% (p=0.91; Mann-Whitney *U*-test; Figure 8C).

3.5 The volume of individual mitochondrial elements based on fluorescent and electron microscopic analysis techniques

Volume measurements of individual mitochondrial elements were equivalent when assessed using either technique. Based on deconvolved images of MitoTracker Red labeled mitochondria, individual mitochondrion elements had a volume of 12.4 ± 1.7 μm^3 with a median of 1.1 μm^3. Based on serial blockface EM images and Calvalieri sampling the volume of individual mitochondrion elements was 11.1 ± 6.6 μm^3 with a median of 1.3 μm^3 (p=0.62; Mann Whitney U-test; Figure 9A).

The frequency distribution of mitochondrial volumes was different between the two techniques, with a marked increase in the percentage of smaller mitochondrial elements in serial blockface EM images as compared to confocal imaging of MitoTracker Red labeled mitochondria ($p<0.0001$, Kolmogorov-Smirnov test; Figure 9B).

3.6 The shape factors of individual mitochondrial elements based on fluorescent and electron microscopic analysis techniques

The aspect ratio was obtained for each mitochondrial element by dividing the longest axis by the shortest axis in both MitoTracker Red confocal microscopic and serial blockface EM images. We did not detect a difference in the aspect ratios of individual mitochondrial elements ($P=0.13$; Mann Whitney U-test; Figure 10A) when comparing confocal fluorescent (3.80 ± 0.02, median=3.17) to 3-dimenisonal EM techniques (5.96 ± 0.02, median=5.59). When the mean aspect ratio of mitochondria within each individual motor neuron was compared, we observed no differences between labeled phrenic motor neurons assessed using MitoTracker Red (3.69 ± 0.14, median=3.34) or putative phrenic motor neurons assessed with EM (3.47 ± 0.51, median=3.28; $P=0.37$; Mann Whitney U-test).

A sphericity or circularity measurement was obtained for each mitochondrial element in MitoTracker Red confocal and serial blockface EM images, respectively. These dimensionless measures quantify the irregularity of mitochondrial morphologies. There was an ~8% difference in the sphericity/circularity of individual mitochondrial elements ($p<0.0001$; Mann Whitney U-test; Figure 10B) when comparing fluorescent (0.63 ± 0.001, median=0.64) to EM techniques (0.58 ± 0.01, median=0.59). When the mean sphericity/circularity of mitochondria within each individual motor neuron was compared, we observed no differences between labeled phrenic motor neurons assessed with MitoTracker Red (0.67 ± 0.01, median=0.67) or putative phrenic motor neurons assessed with EM (0.66 ± 0.04, median=0.65; $P=0.44$; Mann Whitney U-test).

3.7 Dendritic mitochondrial volume density and mitochondrial morphology.

Within a subset of CTB labeled phrenic motor neurons where primary and secondary dendrites could be unambiguously identified and traced to a particular soma (Figure 11A), mitochondrial volume density was assessed, together with mean mitochondrial aspect ratio, mean mitochondrial sphericity and the mean volume of an individual mitochondrial element (Figure 11 A and C). These measurements were compared in a pairwise fashion to equivalent measurements from the somal compartment of that same labeled phrenic motor neuron (Figure 11 A and B). We observed an ~60% reduction in the mitochondrial volume density of primary and secondary dendrites (5.02 ± 1.54) compared to phrenic motor neuron soma (13.13 ± 3.85; $P=0.0004$, Student's paired t-test; Figure 11D). We observed no difference in the aspect ratio of mitochondrial elements from primary and secondary dendrites (2.55 ± 0.15) compared to phrenic motor neuron soma (2.57 ± 0.19; $P=0.56$, Wilcoxon test; Figure 11E). We observed no difference in the sphericity of mitochondrial elements from primary and secondary dendrites (0.59 ± 0.20) compared to phrenic motor neuron soma (1.55 ± 0.55; $P=0.17$, Student's paired t-test; Figure 11F). We observed an ~61% reduction in the mean volume of mitochondrial elements of primary and secondary

dendrites (5.02 ± 1.54) compared to mitochondrial elements within phrenic motor neuron somas (13.13 ± 3.85; P=0.0001, Wilcoxon test; Figure 11G).

3.8 Mitochondrial volume density estimates are repeatable and robust across samples from multiple rodents and between sexes.

The intrathecal application of MitoTracker Red led to a reliable fluorescent signal throughout the spinal cord, including portions with an absence of labeled phrenic motor neurons (top row, Figure 12). We also observed little non-specific fluorescence on the 575-630 nm fluorescence channel when an Alexa 488-conjugated labeled phrenic motor neuron was imaged without any intrathecal application of MitoTracker Red (i.e., a negative control; Figure 12).

The range of mitochondrial volume densities within labeled phrenic motor neurons in rats was ~1-29%. There was no difference in the mean mitochondrial volume density for phrenic motor neurons when compared across rats (P=0.18; Kruskal-Wallis test; Figure 13), with mean values ranging from ~7.5 to 11.0% and medians ranging from ~6 to 10% volume density.

We observed no effect of sex on somal mitochondrial volume density (P=0.73), aspect ratio (P=0.90) or sphericity (P=0.33; Table 1). We also observed no differences between female and males with regard to phrenic motor neuron dendritic mitochondrial volume density (P=0.79; Table 1).

4. DISCUSSION

In the present study, we validated a robust technique that utilizes confocal imaging and semi-automated processing to quantify the volume density of mitochondria in retrogradely-labeled phrenic motor neurons. This novel method allows for quantification of mitochondrial volume density in a larger number of unambiguously identified phrenic motor neurons. We validated this technique by comparison to EM imaging, which is the widely accepted gold standard for imaging mitochondria. We report six main findings: i) intrathecal administration of MitoTracker Red reliably labels mitochondria throughout the cervical spinal cord; ii) when combined with CTB labeling of phrenic motor neurons, mitochondrial volume density within this specific motor neuron pool can be determined; iii) mitochondrial volume density in phrenic motor neurons measured using our novel confocal imaging technique is equivalent to that estimated using serial blockface EM imaging; iv) morphological measurements of individual mitochondrial elements (volume, aspect ratio and sphericity/circularity) identified with our surface detection algorithm exhibit a similar range, median and mean volume when compared to estimates derived from EM imaging, although serial blockface EM was able to distinguish smaller and more irregularly shaped mitochondria; v) mitochondrial volume density is reduced in the dendritic compartment, compared to phrenic motor neuron somas; and vi) mitochondrial volume density estimates utilizing MitoTracker Red were repeatable and robust across rats.

Mitochondrial volume densities and morphologies have been investigated in a plethora of cell types and are particularly sensitive to insults to homeostasis and processes such as

inflammation (Aravamudan et al., 2017; Delmotte et al., 2017; Delmotte and Sieck, 2019; Eisner et al., 2017). In neurons, mitochondria have been a focus of intense interest, as functional and morphological mitochondrial abnormalities have been increasingly implicated in the etiology and propagation of various neurological and neurodegenerative diseases (Dupuis et al., 2004; Hauser and Hastings, 2013; Hirai et al., 2001), including those of motor neurons, such as ALS (Bendotti et al., 2001; Fogarty et al., 2017b; Martin et al., 2007; Sasaki et al., 2004; Sasaki and Iwata, 2007; Wong et al., 1995). In motor neurons, the analysis of mitochondrial morphology under normal conditions has been relatively ignored. Indeed, the interpretation of what is 'normal' mitochondrial morphology is confounded by their nature as dynamic organelles, undergoing continuous cycles of fusion and fission and changes in density in response to homeostatic demands (Bereiter-Hahn and Voth, 1994; Forman et al., 1987; Prakash et al., 2017). Instead, these past efforts have paid great attention to pathological abnormalities of motor neurons, such as vacuolations and breakdown of internal and external mitochondrial membranes, but typically do not assess mitochondrial volume density, nor pay attention to specific motor unit pools (Bendotti et al., 2001; Fogarty et al., 2017b; Martin et al., 2007; Sasaki et al., 2004; Sasaki and Iwata, 2007; Wong et al., 1995).

In this study, we assumed that the net mitochondrial volume density of a phrenic motor neuron reflects mitochondrial abundance, provides useful information regarding overall mitochondrial morphology and can be used as a surrogate for the capacity of mitochondria to produce ATP and meet energy demand. We used MitoTracker Red to label mitochondria because of its stability following fixation (Sorvina et al., 2018) and its extensive use and validation in cultured motor neurons (both primary and NSC-34) (Farrawell et al., 2018; Kalmar et al., 2017; Magrane et al., 2009; Magrane et al., 2012). In other cell types, the overall mitochondrial volume density remains stable within the cell regardless of morphological dynamics, including mitochondrial fusion and mitochondrial fission and the tethering and untethering of mitochondria to the endoplasmic reticulum (Bereiter-Hahn and Voth, 1994; Forman et al., 1987; Prakash et al., 2017). Although we did not expect a brief anesthetised state to affect our volume density assessments past reports on cells in cultured monolayers have reported an effect of ketamine on neuronal mitochondria (Ito et al., 2015), particularly in cultures derived from neonates (Bosnjak et al., 2012; Slikker et al., 2007; Young et al., 2005). Notably, the serum concentrations (~40 μm) of ketamine in ketamine/xylazine anesthetised (with 80-125 mg/kg ketamine dose) rats (Veilleux-Lemieux et al., 2012; Veilleux-Lemieux et al., 2013) does not approach concentrations required for mitochondrial disturbance in cultured neurons, i.e., greater than ~80 μM (Bai et al., 2013; Ito et al., 2015). Irrespective of any potential effect, the animals used for both EM and MitoTracker fluorescent methods were exposed to the same doses of ketamine/xylazine for approximately the same amount of time (see Methods). Similarly, a subset of rats used in the EM studies and all rats used in the fluorescent MitoTracker technique had phrenic motor neurons labelled with CTB. In past studies, we have not observed any changes in phrenic motor neuron discharge (assessed by electromyography *in vivo*) following CTB labeling (Gransee et al., 2013, 2015; Rana et al., 2020). In tissue culture, the CTB used for labeling has been shown to be nontoxic in motor neuron-like NSC-34 cells (Gonzalez Porras et al.,

2016). Taken together, there is no evidence that CTB had any effect on motor neuron activity or mitochondrial volume density.

In motor units (the motor neuron and all of its innervated skeletal muscle fibers), the discharge properties of motor neurons are matched with the activation of constituent muscle fibers. In rat DIAm fibers, innervated by phrenic motor neurons within C_{3-5} spinal cord segments (Fogarty et al., 2018b; Prakash et al., 1994; Rana et al., 2017; Song et al., 2000), mitochondrial volume density ranges between ~2-28% (Sieck et al., 1998). Notably, as a highly active muscle, due to the incessant requirement for breathing (Fogarty et al., 2018a; Fogarty and Sieck, 2019b, a; Khurram et al., 2018b; Mantilla and Sieck, 2011; Sieck, 1991), the mitochondrial volume density in DIAm fibers is greater than that of other muscles without such high ATP demand (Blanco et al., 1991; Conley et al., 1987; Hoppeler et al., 1981; Hoppeler et al., 1987). Accordingly, we expected that in identified phrenic motor neurons, ATP demands would be similar; in agreement, mitochondrial volume density in phrenic motor neurons exhibits a similar 10-fold range (i.e., between ~1-29%). The new MitoTraker Red estimates of mitochondrial volume densities within motor neurons from spinal cord segments C_{3-5} were compared to those obtained using the more established serial blockface EM technique. Our results show a robust overlap between the two techniques, with mean mitochondrial volume densities of 9.3% and 8.9% for MitoTracker Red and EM techniques, respectively. In addition, the volume densities we found using serial blockface EM are similar to those found in mouse lumbar motor neurons during the first two-weeks of life, with mean mitochondrial volume density of lumbar motor neurons being ~10-12% (Miller et al., 2016). Notably, motor neurons at this age are immature in size, with the volume of the motor neuron soma expanding considerably from ~P28 to adulthood (Prakash et al., 2000). Thus, the large range of mitochondrial volume density observed in the present study likely reflects the disparate expansion in size following postnatal development of the adult phrenic motor neurons that comprise the fast fatigue-intermediate and fast-fatigable diaphragm motor units (Fogarty and Sieck, 2019b; Prakash et al., 2000; Sieck, 1991).

To further validate the reliability of the fluorescent MitoTracker Red technique compared to serial blockface EM, we compared the morphometry (individual volume, aspect ratio and sphericity/circularity) of individual mitochondrial elements measured with both techniques. The mean volume of individual mitochondrial elements was not different between the two techniques. However, the distribution of individual mitochondrial volumes differed, with a shift in the cumulative frequency distribution of individual mitochondrial volumes towards smaller mitochondria when assessed by serial blockface EM. For the aspect ratio, individual mitochondria were not different between either technique, indicating that the range of long- and short-axes measured using either techniques was equivalent. By contrast, for the sphericity/circularity measurement, there was a slight (~8%) reduction in the sphericity/circularity of mitochondria assessed via the serial blockface EM method, indicating that the mitochondria assessed this way were marginally more irregular. These small differences in morphometry are readily explained by the difference in spatial resolution and point discrimination between light microscopy and EM. Despite deconvolving the MitoTracker red signal, it is highly likely that we are not able to adequately distinguish between two closely adjacent or juxta-membranous mitochondria (Rana et al., 2019a), when compared to EM. To illustrate this, Figure 7 shows examples of where the membranes of two distinct

mitochondria appear without separation. Using MitoTracker red, these two mitochondria would appear as a contiguous single element and thus skew these morphometric properties towards larger, more regularly shaped mitochondria.

Although our fluorescent imaging of individual mitochondria with MitoTracker Red is limited when compared with EM techniques, the mitochondrial volume estimate was similar to the putative phrenic motor neuron volume density, and is in good agreement with previous estimates of mouse lumbar motor neuron mitochondrial volume density (Miller et al., 2016). Across rats, the range, mean and median mitochondrial volume densities within labeled phrenic motor neurons was repeatable and robust. Using our stereological sampling scheme, there was no difference in the mean and median mitochondrial volume densities among rats used in this study.

Compared to phrenic motor neuron somas, we found a reduction in the mitochondrial volume density and the volume of individual mitochondrial elements in primary and secondary dendrites. We interpret this as reflective of the reduced ATP requirement in dendrites compared to somas, particularly in relation to somal requirements for protein synthesis and action potential generation with overall volume density likely to underpin the ATP production capacity (Ryan et al., 2015; Ryan et al., 2018). By contrast to our present study, past work in dendrites has focused on structural features including fission, fusion, swelling and vacuolation, rather than numerical density (Arnold et al., 2011; Fogarty et al., 2017b; Kalmar et al., 2017; Kong and Xu, 1998; Natale et al., 2015; Parone et al., 2013). In dendrites, the ATP demand required by synaptic activity may be provisioned by mitochondria at post-synaptic sites such as dendritic spines (Li et al., 2004; Rangaraju et al., 2014; Rangaraju et al., 2019). Our current observation of lower dendritic mitochondrial volume density may relate to the relative paucity of dendritic spines on motor neurons (Bandaru et al., 2015; Fogarty et al., 2017b; Kanjhan et al., 2016; Patwa et al., 2019) compared to other types of neurons (e.g., hippocampus CA1 and pyramidal neurons from various neuroanatomical locations) that are more *de rigueur* in studies of mitochondria and/or synaptic plasticity (Brandt et al., 2020; Fogarty et al., 2015a; Fogarty et al., 2016b; Fogarty et al., 2016c; Kasthuri et al., 2015; Klenowski et al., 2017; Li et al., 2004; Popov et al., 2005; Rangaraju et al., 2014; Rangaraju et al., 2019; Sun et al., 2013; Sung et al., 2008). Alternatively, past studies have shown that although the dendritic mitochondrial filaments may be incredibly long (>50 μm in length) (Chicurel and Harris, 1992; Lewis et al., 2018; Popov et al., 2005), their cross sections may are much smaller in diameter (<100 nm) (Kasthuri et al., 2015; Popov et al., 2005), precluding observation using conventional confocal microscopy.

Our technique provides two major advances on previous work. Firstly, we unambiguously identified an entire discrete motor neuron pool, the phrenic, via intrapleural retrograde labeling with CTB (Mantilla et al., 2009). This allows our estimates of mitochondrial volume density to be related to a selective set of DIAm motor units, for which we have an abundance of information regarding their physiological activity during different behaviors. For the DIAm, it is possible to transect the phrenic nerve or the C_2 spinal cord on one side without affecting ventilation (Khurram et al., 2018a; Miyata et al., 1995; Rana et al., 2020; Zhan et al., 1997), and thus lesion studies looking at specific mitochondrial responses to

altered activation and activity patterns are greatly enhanced. Secondly, our MitoTracker red technique is amenable to collecting larger data sets compared to the limited sampling provided by EM. The sheer number of phrenic motor neurons identified following CTB labeling (~400 in rats), dwarfs that which is readily accessible for sampling using serial blockface EM.

Future developments could combine measurement of mitochondrial volume density with quantification of oxidative capacity (e.g., succinate dehydrogenase methods (Blanco et al., 1995; Fogarty et al., 2020a; Ishihara et al., 1995; Ishihara et al., 2001; Sieck and Blanco, 1991) and ATP and oxygen consumption assessments (Miyata and Kawai, 1991, 1992; Ryan et al., 2018; Sickles and McLendon, 1983; Sickles and Oblak, 1983; Sieck et al., 2007) as motor neurons may be predisposed to dysfunction, due to their high activity levels and requirements for ATP. For example, the extreme somato-dendritic to axon polarisation of motor neurons requires ~1.25 x 10^8 molecules of ATP for the anterograde transport of one vesicle along 1 m length of axon (Maday et al., 2014).

In conclusion, we present a reliable and robust methodology for sampling mitochondrial volume density within an identified pool of phrenic motor neurons. This technique is amenable to stereological sampling and is equivalent to the ‘gold standard’ EM method with regards to mitochondrial volume density. We envisage that it will also be possible to probe differences in mitochondrial volume density in other motor neuron pools identified by retrograde labeling in a similar manner.

Acknowledgements:

We would like to thank Rebecca Macken, Yun-Hua Fang, Philippe Delmotte and Wen-Zhi Zhan for their assistance in the completion of this project. Technical assistance for SBEM was provided by Adam Jaspersen and Trace Christensen.

Funding: Supported by National Institutes of Health grants R01-AG044615 (GCS and CBM), R01-AG057052 (CBM and GCS) and R01-HL146114 (GCS and CBM). MJF is the recipient of a National Health and Medical Research Council Early Career (CJ Martin) Fellowship.

REFERENCES

Alvarez-Argote S, Gransee HM, Mora JC, Stowe JM, Jorgenson AJ, Sieck GC, Mantilla CB, 2016. The Impact of Midcervical Contusion Injury on Diaphragm Muscle Function. J Neurotrauma 33, 500–509. 10.1089/neu.2015.4054 [PubMed: 26413840]

Aravamudan B, Kiel A, Freeman M, Delmotte P, Thompson M, Vassallo R, Sieck GC, Pabelick CM, Prakash YS, 2014. Cigarette smoke-induced mitochondrial fragmentation and dysfunction in human airway smooth muscle. Am J Physiol Lung Cell Mol Physiol 306, L840–854. 10.1152/ajplung.00155.2013 [PubMed: 24610934]

Aravamudan B, Thompson M, Sieck GC, Vassallo R, Pabelick CM, Prakash YS, 2017. Functional Effects of Cigarette Smoke-Induced Changes in Airway Smooth Muscle Mitochondrial Morphology. J Cell Physiol 232, 1053–1068. 10.1002/jcp.25508 [PubMed: 27474898]

Arnold B, Cassady SJ, VanLaar VS, Berman SB, 2011. Integrating multiple aspects of mitochondrial dynamics in neurons: age-related differences and dynamic changes in a chronic rotenone model. Neurobiol Dis 41, 189–200. 10.1016/j.nbd.2010.09.006 [PubMed: 20850532]

Bai X, Yan Y, Canfield S, Muravyeva MY, Kikuchi C, Zaja I, Corbett JA, Bosnjak ZJ, 2013. Ketamine enhances human neural stem cell proliferation and induces neuronal apoptosis via reactive oxygen

species-mediated mitochondrial pathway. Anesth Analg 116, 869–880. 10.1213/ANE.0b013e3182860fc9 [PubMed: 23460563]

Bandaru SP, Liu S, Waxman SG, Tan AM, 2015. Dendritic spine dysgenesis contributes to hyperreflexia after spinal cord injury. J Neurophysiol 113, 1598–1615. 10.1152/jn.00566.2014 [PubMed: 25505110]

Banks GB, Kanjhan R, Wiese S, Kneussel M, Wong LM, O'Sullivan G, Sendtner M, Bellingham MC, Betz H, Noakes PG, 2005. Glycinergic and GABAergic synaptic activity differentially regulate motoneuron survival and skeletal muscle innervation.[Erratum appears in J Neurosci. 2005 Mar 16;25(11):3018-21]. Journal of Neuroscience 25, 1249–1259. [PubMed: 15689563]

Bendotti C, Calvaresi N, Chiveri L, Prelle A, Moggio M, Braga M, Silani V, De Biasi S, 2001. Early vacuolization and mitochondrial damage in motor neurons of FALS mice are not associated with apoptosis or with changes in cytochrome oxidase histochemical reactivity. J Neurol Sci 191, 25–33. 10.1016/s0022-510x(01)00627-x [PubMed: 11676989]

Bereiter-Hahn J, Voth M, 1994. Dynamics of mitochondria in living cells: shape changes, dislocations, fusion, and fission of mitochondria. Microsc Res Tech 27, 198–219. 10.1002/jemt.1070270303 [PubMed: 8204911]

Blanco CE, Fournier M, Sieck GC, 1991. Metabolic variability within individual fibres of the cat tibialis posterior and diaphragm muscles. Histochemical Journal 23, 366–374.

Blanco CE, Micevych PE, Zhan WZ, Sieck GC, 1995. Succinate dehydrogenase activity of sexually dimorphic muscles of rats. J Appl Physiol 78, 2147–2152. [PubMed: 7665411]

Bosnjak ZJ, Yan Y, Canfield S, Muravyeva MY, Kikuchi C, Wells CW, Corbett JA, Bai X, 2012. Ketamine induces toxicity in human neurons differentiated from embryonic stem cells via mitochondrial apoptosis pathway. Curr Drug Saf 7, 106–119. 10.2174/157488612802715663 [PubMed: 22873495]

Brandenburg JE, Fogarty MJ, Brown AD, Sieck GC, 2020. Phrenic motor neuron loss in an animal model of early onset hypertonia. J Neurophysiol 123, 1682–1690. 10.1152/jn.00026.2020 [PubMed: 32233911]

Brandenburg JE, Gransee HM, Fogarty MJ, Sieck GC, 2018. Differences in Lumbar Motor Neuron Pruning in an Animal Model of Early Onset Spasticity. J Neurophysiol 120, 601–609. 10.1152/jn.00186.2018 [PubMed: 29718808]

Brandt N, Loffler T, Fester L, Rune GM, 2020. Sex-specific features of spine densities in the hippocampus. Sci Rep 10, 11405. 10.1038/s41598-020-68371-x [PubMed: 32647191]

Campa JF, Engel WK, 1970. Histochemistry of motor neurons and interneurons in the cat lumbar spinal cord. Neurology 20, 559–568. [PubMed: 4192908]

Chicurel ME, Harris KM, 1992. Three-dimensional analysis of the structure and composition of CA3 branched dendritic spines and their synaptic relationships with mossy fiber boutons in the rat hippocampus. J Comp Neurol 325, 169–182. 10.1002/cne.903250204 [PubMed: 1460112]

Conley KE, Kayar SR, Rosler K, Hoppeler H, Weibel ER, Taylor CR, 1987. Adaptive variation in the mammalian respiratory system in relation to energetic demand: IV. Capillaries and their relationship to oxidative capacity. Respir Physiol 69, 47–64.

Delmotte P, Sieck GC, 2019. Endoplasmic Reticulum Stress and Mitochondrial Function in Airway Smooth Muscle. Front Cell Dev Biol 7, 374. 10.3389/fcell.2019.00374 [PubMed: 32010691]

Delmotte P, Zavaletta VA, Thompson MA, Prakash YS, Sieck GC, 2017. TNFalpha decreases mitochondrial movement in human airway smooth muscle. Am J Physiol Lung Cell Mol Physiol 313, L166–L176. 10.1152/ajplung.00538.2016 [PubMed: 28473328]

Delmotte PF, Marin Mathieu N, Sieck GC, 2020. TNFalpha Induces Mitochondrial Fragmentation and Biogenesis in Human Airway Smooth Muscle. Am J Physiol Lung Cell Mol Physiol. 10.1152/ajplung.00305.2020

Deng HX, Shi Y, Furukawa Y, Zhai H, Fu R, Liu E, Gorrie GH, Khan MS, Hung WY, Bigio EH, Lukas T, Dal Canto MC, O'Halloran TV, Siddique T, 2006. Conversion to the amyotrophic lateral sclerosis phenotype is associated with intermolecular linked insoluble aggregates of SOD1 in mitochondria. Proc Natl Acad Sci U S A 103, 7142–7147. 10.1073/pnas.0602046103 [PubMed: 16636275]

Dupuis L, Gonzalez de Aguilar JL, Oudart H, de Tapia M, Barbeito L, Loeffler JP, 2004. Mitochondria in amyotrophic lateral sclerosis: a trigger and a target. Neurodegener Dis 1, 245–254. 10.1159/000085063 [PubMed: 16908975]

Eisner V, Cupo RR, Gao E, Csordas G, Slovinsky WS, Paillard M, Cheng L, Ibetti J, Chen SR, Chuprun JK, Hoek JB, Koch WJ, Hajnoczky G, 2017. Mitochondrial fusion dynamics is robust in the heart and depends on calcium oscillations and contractile activity. Proc Natl Acad Sci U S A 114, E859–E868. 10.1073/pnas.1617288114 [PubMed: 28096338]

Farrawell NE, Lambert-Smith I, Mitchell K, McKenna J, McAlary L, Ciryam P, Vine KL, Saunders DN, Yerbury JJ, 2018. SOD1(A4V) aggregation alters ubiquitin homeostasis in a cell model of ALS. J Cell Sci 131. 10.1242/jcs.209122

Fogarty MJ, Gonzalez Porras MA, Mantilla CB, Sieck GC, 2019a. Diaphragm neuromuscular transmission failure in aged rats. J Neurophysiol 122, 93–104. 10.1152/jn.00061.2019 [PubMed: 31042426]

Fogarty MJ, Hammond LA, Kanjhan R, Bellingham MC, Noakes PG, 2013a. A method for the three-dimensional reconstruction of Neurobiotin-filled neurons and the location of their synaptic inputs. Front Neural Circuits 7, 153. 10.3389/fncir.2013.00153 [PubMed: 24101895]

Fogarty MJ, Kanjhan R, Bellingham MC, Noakes PG, 2016a. Glycinergic Neurotransmission: A Potent Regulator of Embryonic Motor Neuron Dendritic Morphology and Synaptic Plasticity. J Neurosci 36, 80–87. 10.1523/JNEUROSCI.1576-15.2016 [PubMed: 26740651]

Fogarty MJ, Kanjhan R, Yanagawa Y, Noakes PG, Bellingham MC, 2017a. Alterations in hypoglossal motor neurons due to GAD67 and VGAT deficiency in mice. Exp Neurol 289, 117–127. 10.1016/j.expneurol.2016.12.004 [PubMed: 27956032]

Fogarty MJ, Klenowski PM, Lee JD, Drieberg-Thompson JR, Bartlett SE, Ngo ST, Hilliard MA, Bellingham MC, Noakes PG, 2016b. Cortical synaptic and dendritic spine abnormalities in a presymptomatic TDP-43 model of amyotrophic lateral sclerosis. Sci Rep 6, 37968. 10.1038/srep37968 [PubMed: 27897242]

Fogarty MJ, Mantilla CB, Sieck GC, 2018a. Breathing: Motor Control of Diaphragm Muscle. Physiology (Bethesda) 33, 113–126. 10.1152/physiol.00002.2018 [PubMed: 29412056]

Fogarty MJ, Mantilla CB, Sieck GC, 2019b. Impact of sarcopenia on diaphragm muscle fatigue. Exp Physiol 104, 1090–1099. 10.1113/EP087558 [PubMed: 30924589]

Fogarty MJ, Marin Mathieu N, Mantilla CB, Sieck GC, 2020a. Aging Reduces Succinate Dehydrogenase Activity in Rat Type IIx/IIb Diaphragm Muscle Fibers. J Appl Physiol (1985). 10.1152/japplphysiol.00644.2019

Fogarty MJ, Mu EW, Noakes PG, Lavidis NA, Bellingham MC, 2016c. Marked changes in dendritic structure and spine density precede significant neuronal death in vulnerable cortical pyramidal neuron populations in the SOD1(G93A) mouse model of amyotrophic lateral sclerosis. Acta Neuropathol Commun 4, 77. 10.1186/s40478-016-0347-y [PubMed: 27488828]

Fogarty MJ, Mu EWH, Lavidis NA, Noakes PG, Bellingham MC, 2017b. Motor Areas Show Altered Dendritic Structure in an Amyotrophic Lateral Sclerosis Mouse Model. Front Neurosci 11, 609. 10.3389/fnins.2017.00609 [PubMed: 29163013]

Fogarty MJ, Mu EWH, Lavidis NA, Noakes PG, Bellingham MC, 2020b. Size-Dependent Vulnerability of Lumbar Motor Neuron Dendritic Degeneration in SOD1(G93A) Mice. Anat Rec (Hoboken) 303, 1455–1471. 10.1002/ar.24255 [PubMed: 31509351]

Fogarty MJ, Noakes PG, Bellingham MC, 2015a. Motor cortex layer V pyramidal neurons exhibit dendritic regression, spine loss, and increased synaptic excitation in the presymptomatic hSOD1(G93A) mouse model of amyotrophic lateral sclerosis. J Neurosci 35, 643–647. 10.1523/JNEUROSCI.3483-14.2015 [PubMed: 25589758]

Fogarty MJ, Omar TS, Zhan WZ, Mantilla CB, Sieck GC, 2018b. Phrenic Motor Neuron Loss in Aged Rats. J Neurophysiol 119, 1852–1862. 10.1152/jn.00868.2017 [PubMed: 29412773]

Fogarty MJ, Sieck GC, 2019a. Diaphragm muscle adaptations in health and disease. Drug Discovery Today: Disease Models In Press.

Fogarty MJ, Sieck GC, 2019b. Evolution and Functional Differentiation of the Diaphragm Muscle of Mammals. Compr Physiol 9, 715–766. [PubMed: 30873594]

Fogarty MJ, Smallcombe KL, Yanagawa Y, Obata K, Bellingham MC, Noakes PG, 2013b. Genetic deficiency of GABA differentially regulates respiratory and non-respiratory motor neuron development. PLoS ONE [Electronic Resource] 8, e56257.

Fogarty MJ, Yanagawa Y, Obata K, Bellingham MC, Noakes PG, 2015b. Genetic absence of the vesicular inhibitory amino acid transporter differentially regulates respiratory and locomotor motor neuron development. Brain Struct Funct 220, 525–540. 10.1007/s00429-013-0673-9 [PubMed: 24276495]

Forman DS, Lynch KJ, Smith RS, 1987. Organelle dynamics in lobster axons: anterograde, retrograde and stationary mitochondria. Brain Res 412, 96–106. 10.1016/0006-8993(87)91443-0 [PubMed: 3607465]

Gonzalez Porras MA, Durfee PN, Gregory AM, Sieck GC, Brinker CJ, Mantilla CB, 2016. A novel approach for targeted delivery to motoneurons using cholera toxin-B modified protocells. J Neurosci Methods 273, 160–174. 10.1016/j.jneumeth.2016.09.003 [PubMed: 27641118]

Gonzalez Porras MA, Fogarty MJ, Gransee HM, Sieck GC, Mantilla CB, 2019. Frequency-dependent lipid raft uptake at rat diaphragm muscle axon terminals. Muscle Nerve 59, 611–618. 10.1002/mus.26421 [PubMed: 30677149]

Gransee HM, Zhan WZ, Sieck GC, Mantilla CB, 2013. Targeted Delivery of TrkB Receptor to Phrenic Motoneurons Enhances Functional Recovery of Rhythmic Phrenic Activity after Cervical Spinal Hemisection. PLoS One 8, e64755. 10.1371/journal.pone.0064755 [PubMed: 23724091]

Gransee HM, Zhan WZ, Sieck GC, Mantilla CB, 2015. Localized Delivery of Brain-Derived Neurotrophic Factor-Expressing Mesenchymal Stem Cells Enhances Functional Recovery following Cervical Spinal Cord Injury. J Neurotrauma 32, 185–193. 10.1089/neu.2014.3464 [PubMed: 25093762]

Hart MN, Cancilla PA, Frommes S, Hirano A, 1977. Anterior horn cell degeneration and Bunina-type inclusions associated with dementia. Acta Neuropathol 38, 225–228. 10.1007/bf00688069 [PubMed: 197771]

Hauser DN, Hastings TG, 2013. Mitochondrial dysfunction and oxidative stress in Parkinson's disease and monogenic parkinsonism. Neurobiol Dis 51, 35–42. 10.1016/j.nbd.2012.10.011 [PubMed: 23064436]

Herxheimer H, 1949. Some observations on the coordination of diaphragmatic and rib movement in respiration. Thorax 4, 65–72. 10.1136/thx.4.1.65 [PubMed: 18124450]

Hirai K, Aliev G, Nunomura A, Fujioka H, Russell RL, Atwood CS, Johnson AB, Kress Y, Vinters HV, Tabaton M, Shimohama S, Cash AD, Siedlak SL, Harris PL, Jones PK, Petersen RB, Perry G, Smith MA, 2001. Mitochondrial abnormalities in Alzheimer's disease. J Neurosci 21, 3017–3023. [PubMed: 11312286]

Hirano A, Donnenfeld H, Sasaki S, Nakano I, 1984a. Fine structural observations of neurofilamentous changes in amyotrophic lateral sclerosis. J Neuropathol Exp Neurol 43, 461–470. 10.1097/00005072-198409000-00001 [PubMed: 6540799]

Hirano A, Nakano I, Kurland LT, Mulder DW, Holley PW, Saccomanno G, 1984b. Fine structural study of neurofibrillary changes in a family with amyotrophic lateral sclerosis. J Neuropathol Exp Neurol 43, 471–480. 10.1097/00005072-198409000-00002 [PubMed: 6540800]

Hoppeler H, Hudlicka O, Uhlmann E, 1987. Relationship between mitochondria and oxygen consumption in isolated cat muscles. J Physiol 385, 661–675. [PubMed: 3309266]

Hoppeler H, Mathieu O, Krauer R, Claassen H, Armstrong RB, Weibel ER, 1981. Design of the mammalian respiratory system. VI. Distribution of mitochondria and capillaries in various muscles. Respir Physiol 44, 87–111. [PubMed: 7232888]

Ishihara A, Ohira Y, Tanaka M, Nishikawa W, Ishioka N, Higashibata A, Izumi R, Shimazu T, Ibata Y, 2001. Cell body size and succinate dehydrogenase activity of spinal motoneurons innervating the soleus muscle in mice, rats, and cats. Neurochem Res 26, 1301–1304. 10.1023/a:1014245417017 [PubMed: 11885781]

Ishihara A, Roy RR, Edgerton VR, 1995. Succinate dehydrogenase activity and soma size of motoneurons innervating different portions of the rat tibialis anterior. Neuroscience 68, 813–822. 10.1016/0306-4522(95)00165-f [PubMed: 8577376]

Issa AN, Zhan WZ, Sieck G, Mantilla CB, 2010. Neuregulin-1 at synapses on phrenic motoneurons. J Comp Neurol 518, 4213–4225. [PubMed: 20878784]

Ito H, Uchida T, Makita K, 2015. Ketamine causes mitochondrial dysfunction in human induced pluripotent stem cell-derived neurons. PLoS One 10, e0128445. 10.1371/journal.pone.0128445 [PubMed: 26020236]

Jaarsma D, Haasdijk ED, Grashorn JA, Hawkins R, van Duijn W, Verspaget HW, London J, Holstege JC, 2000. Human Cu/Zn superoxide dismutase (SOD1) overexpression in mice causes mitochondrial vacuolization, axonal degeneration, and premature motoneuron death and accelerates motoneuron disease in mice expressing a familial amyotrophic lateral sclerosis mutant SOD1. Neurobiol Dis 7, 623–643. 10.1006/nbdi.2000.0299 [PubMed: 11114261]

Kalmar B, Innes A, Wanisch K, Kolaszynska AK, Pandraud A, Kelly G, Abramov AY, Reilly MM, Schiavo G, Greensmith L, 2017. Mitochondrial deficits and abnormal mitochondrial retrograde axonal transport play a role in the pathogenesis of mutant Hsp27-induced Charcot Marie Tooth Disease. Hum Mol Genet 26, 3313–3326. 10.1093/hmg/ddx216 [PubMed: 28595321]

Kanjhan R, Fogarty MJ, Noakes PG, Bellingham MC, 2016. Developmental changes in the morphology of mouse hypoglossal motor neurons. Brain Struct Funct 221, 3755–3786. 10.1007/s00429-015-1130-8 [PubMed: 26476929]

Kasthuri N, Hayworth KJ, Berger DR, Schalek RL, Conchello JA, Knowles-Barley S, Lee D, Vazquez-Reina A, Kaynig V, Jones TR, Roberts M, Morgan JL, Tapia JC, Seung HS, Roncal WG, Vogelstein JT, Burns R, Sussman DL, Priebe CE, Pfister H, Lichtman JW, 2015. Saturated Reconstruction of a Volume of Neocortex. Cell 162, 648–661. 10.1016/j.cell.2015.06.054 [PubMed: 26232230]

Khurram OU, Fogarty MJ, Rana S, Vang P, Sieck GC, Mantilla CB, 2018a. Diaphragm muscle function following mid-cervical contusion injury in rats. J Appl Physiol (1985). 10.1152/japplphysiol.00481.2018

Khurram OU, Fogarty MJ, Sarrafian TL, Bhatt A, Mantilla CB, Sieck GC, 2018b. Impact of aging on diaphragm muscle function in male and female Fischer 344 rats. Physiol Rep 6, e13786. 10.14814/phy2.13786 [PubMed: 29981218]

Klenowski PM, Fogarty MJ, Belmer A, Noakes PG, Bellingham MC, Bartlett SE, 2015. Structural and functional characterization of dendritic arbors and GABAergic synaptic inputs on interneurons and principal cells in the rat basolateral amygdala. J Neurophysiol 114, 942–957. 10.1152/jn.00824.2014 [PubMed: 26041829]

Klenowski PM, Wright SE, Mu EWH, Noakes PG, Lavidis NA, Bartlett SE, Bellingham MC, Fogarty MJ, 2017. Investigating Methodological Differences in the Assessment of Dendritic Morphology of Basolateral Amygdala Principal Neurons-A Comparison of Golgi-Cox and Neurobiotin Electroporation Techniques. Brain Sci 7. 10.3390/brainsci7120165

Kong J, Xu Z, 1998. Massive mitochondrial degeneration in motor neurons triggers the onset of amyotrophic lateral sclerosis in mice expressing a mutant SOD1. J Neurosci 18, 3241–3250. [PubMed: 9547233]

Koopman WJ, Visch HJ, Verkaart S, van den Heuvel LW, Smeitink JA, Willems PH, 2005. Mitochondrial network complexity and pathological decrease in complex I activity are tightly correlated in isolated human complex I deficiency. American journal of physiology. Cell physiology 289, C881–890. 10.1152/ajpcell.00104.2005 [PubMed: 15901599]

Lance-Jones C, 1982. Motoneuron cell death in the developing lumbar spinal cord of the mouse. Brain Res 256, 473–479. 10.1016/0165-3806(82)90192-4 [PubMed: 7127154]

Leduc-Gaudet JP, Picard M, St-Jean Pelletier F, Sgarioto N, Auger MJ, Vallee J, Robitaille R, St-Pierre DH, Gouspillou G, 2015. Mitochondrial morphology is altered in atrophied skeletal muscle of aged mice. Oncotarget 6, 17923–17937. 10.18632/oncotarget.4235 [PubMed: 26053100]

Lewis TL Jr., Kwon SK, Lee A, Shaw R, Polleux F, 2018. MFF-dependent mitochondrial fission regulates presynaptic release and axon branching by limiting axonal mitochondria size. Nat Commun 9, 5008. 10.1038/s41467-018-07416-2 [PubMed: 30479337]

Li Z, Okamoto K, Hayashi Y, Sheng M, 2004. The importance of dendritic mitochondria in the morphogenesis and plasticity of spines and synapses. Cell 119, 873–887. 10.1016/j.cell.2004.11.003 [PubMed: 15607982]

Maday S, Twelvetrees AE, Moughamian AJ, Holzbaur EL, 2014. Axonal transport: cargo-specific mechanisms of motility and regulation. Neuron 84, 292–309. 10.1016/j.neuron.2014.10.019 [PubMed: 25374356]

Magrane J, Hervias I, Henning MS, Damiano M, Kawamata H, Manfredi G, 2009. Mutant SOD1 in neuronal mitochondria causes toxicity and mitochondrial dynamics abnormalities. Hum Mol Genet 18, 4552–4564. 10.1093/hmg/ddp421 [PubMed: 19779023]

Magrane J, Sahawneh MA, Przedborski S, Estevez AG, Manfredi G, 2012. Mitochondrial dynamics and bioenergetic dysfunction is associated with synaptic alterations in mutant SOD1 motor neurons. J Neurosci 32, 229–242. 10.1523/JNEUROSCI.1233-11.2012 [PubMed: 22219285]

Mantilla CB, Gransee HM, Zhan WZ, Sieck GC, 2013. Motoneuron BDNF/TrkB signaling enhances functional recovery after cervical spinal cord injury. Exp Neurol 247C, 101–109. 10.1016/j.expneurol.2013.04.002

Mantilla CB, Sieck GC, 2011. Phrenic motor unit recruitment during ventilatory and non-ventilatory behaviors. Respir Physiol Neurobiol 179, 57–63. https://doi.org/S1569-9048(11)00241-2 [pii] 10.1016/j.resp.2011.06.028 [PubMed: 21763470]

Mantilla CB, Zhan WZ, Gransee HM, Prakash YS, Sieck GC, 2018. Phrenic motoneuron structural plasticity across models of diaphragm muscle paralysis. J Comp Neurol. 10.1002/cne.24503

Mantilla CB, Zhan WZ, Sieck GC, 2009. Retrograde labeling of phrenic motoneurons by intrapleural injection. J Neurosci Methods 182, 244–249. [PubMed: 19559048]

Martin LJ, Liu Z, Chen K, Price AC, Pan Y, Swaby JA, Golden WC, 2007. Motor neuron degeneration in amyotrophic lateral sclerosis mutant superoxide dismutase-1 transgenic mice: mechanisms of mitochondriopathy and cell death. J Comp Neurol 500, 20–46. 10.1002/cne.21160 [PubMed: 17099894]

Miller N, Shi H, Zelikovich AS, Ma YC, 2016. Motor neuron mitochondrial dysfunction in spinal muscular atrophy. Hum Mol Genet 25, 3395–3406. 10.1093/hmg/ddw262 [PubMed: 27488123]

Mitchelle A, Watson C, 2016. The organization of spinal motor neurons in a monotreme is consistent with a six-region schema of the mammalian spinal cord. J Anat 229, 394–405. 10.1111/joa.12492 [PubMed: 27173752]

Miyata H, Kawai Y, 1991. Soma diameter and oxidative enzyme activity of identified alpha-motoneurons: application of a retrograde fluorescent neuronal tracer. Brain Res 544, 141–144. 10.1016/0006-8993(91)90896-4 [PubMed: 1855134]

Miyata H, Kawai Y, 1992. Relationship between soma diameter and oxidative enzyme activity of alpha-motoneurons. Brain Res 581, 101–107. 10.1016/0006-8993(92)90348-d [PubMed: 1498661]

Miyata H, Zhan WZ, Prakash YS, Sieck GC, 1995. Myoneural interactions affect diaphragm muscle adaptations to inactivity. J Appl Physiol 79, 1640–1649. [PubMed: 8594024]

Natale G, Lenzi P, Lazzeri G, Falleni A, Biagioni F, Ryskalin L, Fornai F, 2015. Compartment-dependent mitochondrial alterations in experimental ALS, the effects of mitophagy and mitochondriogenesis. Front Cell Neurosci 9, 434. 10.3389/fncel.2015.00434 [PubMed: 26594150]

Nyengaard JR, Gundersen HJ, 2006. Direct and efficient stereological estimation of total cell quantities using electron microscopy. J Microsc 222, 182–187. 10.1111/j.1365-2818.2006.01586.x [PubMed: 16872417]

Oppenheim RW, 1986. The absence of significant postnatal motoneuron death in the brachial and lumbar spinal cord of the rat. J Comp Neurol 246, 281–286. [PubMed: 3958254]

Parone PA, Da Cruz S, Han JS, McAlonis-Downes M, Vetto AP, Lee SK, Tseng E, Cleveland DW, 2013. Enhancing mitochondrial calcium buffering capacity reduces aggregation of misfolded SOD1 and motor neuron cell death without extending survival in mouse models of inherited amyotrophic lateral sclerosis. J Neurosci 33, 4657–4671. 10.1523/JNEUROSCI.1119-12.2013 [PubMed: 23486940]

Patwa S, Benson CA, Dyer L, Olson KL, Bangalore L, Hill M, Waxman SG, Tan AM, 2019. Spinal cord motor neuron plasticity accompanies second-degree burn injury and chronic pain. Physiol Rep 7, e14288. 10.14814/phy2.14288 [PubMed: 31858746]

Picard M, White K, Turnbull DM, 2013. Mitochondrial morphology, topology, and membrane interactions in skeletal muscle: a quantitative three-dimensional electron microscopy study. J Appl Physiol (1985) 114, 161–171. 10.1152/japplphysiol.01096.2012 [PubMed: 23104694]

Popov V, Medvedev NI, Davies HA, Stewart MG, 2005. Mitochondria form a filamentous reticular network in hippocampal dendrites but are present as discrete bodies in axons: a three-dimensional ultrastructural study. J Comp Neurol 492, 50–65. 10.1002/cne.20682 [PubMed: 16175555]

Prakash YS, Mantilla CB, Zhan WZ, Smithson KG, Sieck GC, 2000. Phrenic motoneuron morphology during rapid diaphragm muscle growth. J Appl Physiol 89, 563–572. [PubMed: 10926639]

Prakash YS, Pabelick CM, Sieck GC, 2017. Mitochondrial Dysfunction in Airway Disease. Chest 152, 618–626. 10.1016/j.chest.2017.03.020 [PubMed: 28336486]

Prakash YS, Smithson KG, Sieck GC, 1993. Measurements of motoneuron somal volumes using laser confocal microscopy: comparisons with shape-based stereological estimations. Neuroimage 1, 95–107. [PubMed: 9343561]

Prakash YS, Smithson KG, Sieck GC, 1994. Application of the Cavalieri principle in volume estimation using laser confocal microscopy. Neuroimage 1, 325–333. [PubMed: 9343582]

Rana S, Mantilla CB, Sieck GC, 2019a. Glutamatergic Input Varies with Phrenic Motor Neuron Size. J Neurophysiol. 10.1152/jn.00430.2019

Rana S, Sieck GC, Mantilla CB, 2017. Diaphragm electromyographic activity following unilateral midcervical contusion injury in rats. J Neurophysiol 117, 545–555. 10.1152/jn.00727.2016 [PubMed: 27832610]

Rana S, Sieck GC, Mantilla CB, 2019b. Heterogeneous glutamatergic receptor mRNA expression across phrenic motor neurons in rats. J Neurochem. 10.1111/jnc.14881

Rana S, Zhan WZ, Mantilla CB, Sieck GC, 2020. Disproportionate loss of excitatory inputs to smaller phrenic motor neurons following cervical spinal hemisection. J Physiol. 10.1113/JP280130

Rangaraju V, Calloway N, Ryan TA, 2014. Activity-driven local ATP synthesis is required for synaptic function. Cell 156, 825–835. 10.1016/j.cell.2013.12.042 [PubMed: 24529383]

Rangaraju V, Lauterbach M, Schuman EM, 2019. Spatially Stable Mitochondrial Compartments Fuel Local Translation during Plasticity. Cell 176, 73–84 e15. 10.1016/j.cell.2018.12.013 [PubMed: 30612742]

Ryan ZC, Craig TA, Folmes CD, Wang X, Lanza IR, Schaible NS, Salisbury JL, Nair KS, Terzic A, Sieck GC, Kumar R, 2015. 1α,25-Dihydroxyvitamin D 3 Regulates Mitochondrial Oxygen Consumption and Dynamics in Human Skeletal Muscle Cells. Journal of Biological Chemistry. 10.1074/jbc.M115.684399

Ryan ZC, Craig TA, Wang X, Delmotte P, Salisbury JL, Lanza IR, Sieck GC, Kumar R, 2018. 1alpha,25-dihydroxyvitamin D3 mitigates cancer cell mediated mitochondrial dysfunction in human skeletal muscle cells. Biochem Biophys Res Commun 496, 746–752. 10.1016/j.bbrc.2018.01.092 [PubMed: 29366785]

Sasaki S, Iwata M, 2007. Mitochondrial alterations in the spinal cord of patients with sporadic amyotrophic lateral sclerosis. J Neuropathol Exp Neurol 66, 10–16. 10.1097/nen.0b013e31802c396b [PubMed: 17204932]

Sasaki S, Warita H, Murakami T, Abe K, Iwata M, 2004. Ultrastructural study of mitochondria in the spinal cord of transgenic mice with a G93A mutant SOD1 gene. Acta Neuropathol 107, 461–474. 10.1007/s00401-004-0837-z [PubMed: 15029445]

Sickles DW, McLendon RE, 1983. Metabolic variation among rat lumbosacral alpha-motoneurons. Histochem 79, 205–217.

Sickles DW, Oblak TG, 1983. A horseradish peroxidase labeling technique for correlation of motoneuron metabolic activity with muscle fiber types. J Neurosci Methods 7, 195–201. [PubMed: 6188929]

Sieck GC, 1991. Neural control of the inspiratory pump. NIPS 6, 260–264.

Sieck GC, Blanco CE, 1991. Postnatal changes in the distribution of succinate dehydrogenase activities among diaphragm muscle fibers. Pediatr Res 29, 586–593. [PubMed: 1830959]

Sieck GC, Fournier M, 1989. Diaphragm motor unit recruitment during ventilatory and nonventilatory behaviors. J Appl Physiol 66, 2539–2545. [PubMed: 2745316]

Sieck GC, Han YS, Prakash YS, Jones KA, 1998. Cross-bridge cycling kinetics, actomyosin ATPase activity and myosin heavy chain isoforms in skeletal and smooth respiratory muscles. Comp Biochem Physiol 119, 435–450.

Sieck GC, Mantilla CB, Prakash YS, 1999. Volume measurements in confocal microscopy. Methods Enzymol 307, 296–315. [PubMed: 10506980]

Sieck GC, Zhan WZ, Han YS, Prakash YS, 2007. Effect of denervation on ATP consumption rate of diaphragm muscle fibers. J Appl Physiol 103, 858–866. [PubMed: 17556500]

Slikker W Jr., Zou X, Hotchkiss CE, Divine RL, Sadovova N, Twaddle NC, Doerge DR, Scallet AC, Patterson TA, Hanig JP, Paule MG, Wang C, 2007. Ketamine-induced neuronal cell death in the perinatal rhesus monkey. Toxicol Sci 98, 145–158. 10.1093/toxsci/kfm084 [PubMed: 17426105]

Slomianka L, 2020. Basic quantitative morphological methods applied to the central nervous system. J Comp Neurol. 10.1002/cne.24976

Song A, Ashwell KW, Tracey DJ, 2000. Development of the rat phrenic nucleus and its connections with brainstem respiratory nuclei. Anat Embryol (Berl) 202, 159–177. [PubMed: 10985434]

Sorvina A, Bader CA, Darby JRT, Lock MC, Soo JY, Johnson IRD, Caporale C, Voelcker NH, Stagni S, Massi M, Morrison JL, Plush SE, Brooks DA, 2018. Mitochondrial imaging in live or fixed tissues using a luminescent iridium complex. Sci Rep 8, 8191. 10.1038/s41598-018-24672-w [PubMed: 29844412]

Steyn FJ, Lee K, Fogarty MJ, Veldhuis JD, McCombe PA, Bellingham MC, Ngo ST, Chen C, 2013. Growth hormone secretion is correlated with neuromuscular innervation rather than motor neuron number in early-symptomatic male amyotrophic lateral sclerosis mice. Endocrinology 154, 4695–4706. 10.1210/en.2013-1570 [PubMed: 24108071]

Sun T, Qiao H, Pan PY, Chen Y, Sheng ZH, 2013. Motile axonal mitochondria contribute to the variability of presynaptic strength. Cell Rep 4, 413–419. 10.1016/j.celrep.2013.06.040 [PubMed: 23891000]

Sung JY, Engmann O, Teylan MA, Nairn AC, Greengard P, Kim Y, 2008. WAVE1 controls neuronal activity-induced mitochondrial distribution in dendritic spines. Proc Natl Acad Sci U S A 105, 3112–3116. 10.1073/pnas.0712180105 [PubMed: 18287015]

Vande Voorde J, Ackermann T, Pfetzer N, Sumpton D, Mackay G, Kalna G, Nixon C, Blyth K, Gottlieb E, Tardito S, 2019. Improving the metabolic fidelity of cancer models with a physiological cell culture medium. Sci Adv 5, eaau7314. 10.1126/sciadv.aau7314 [PubMed: 30613774]

Veilleux-Lemieux D, Beaudry F, Helie P, Vachon P, 2012. Effects of endotoxemia on the pharmacodynamics and pharmacokinetics of ketamine and xylazine anesthesia in Sprague-Dawley rats. Vet Med (Auckl) 3, 99–109. 10.2147/VMRR.S35666 [PubMed: 30101090]

Veilleux-Lemieux D, Castel A, Carrier D, Beaudry F, Vachon P, 2013. Pharmacokinetics of ketamine and xylazine in young and old Sprague-Dawley rats. J Am Assoc Lab Anim Sci 52, 567–570. [PubMed: 24041212]

Wong PC, Pardo CA, Borchelt DR, Lee MK, Copeland NG, Jenkins NA, Sisodia SS, Cleveland DW, Price DL, 1995. An adverse property of a familial ALS-linked SOD1 mutation causes motor neuron disease characterized by vacuolar degeneration of mitochondria. Neuron 14, 1105–1116. 10.1016/0896-6273(95)90259-7 [PubMed: 7605627]

Young C, Jevtovic-Todorovic V, Qin YQ, Tenkova T, Wang H, Labruyere J, Olney JW, 2005. Potential of ketamine and midazolam, individually or in combination, to induce apoptotic neurodegeneration in the infant mouse brain. Br J Pharmacol 146, 189–197. 10.1038/sj.bjp.0706301 [PubMed: 15997239]

Zhan WZ, Mantilla CB, Zhan P, Bitton A, Prakash YS, de Troyer A, Sieck GC, 2000. Regional differences in serotonergic input to canine parasternal intercostal motoneurons. J Appl Physiol 88, 1581–1589. [PubMed: 10797116]

Zhan WZ, Miyata H, Prakash YS, Sieck GC, 1997. Metabolic and phenotypic adaptations of diaphragm muscle fibers with inactivation. J Appl Physiol 82, 1145–1153. [PubMed: 9104851]

Highlights:

- We present a novel mitochondrial labelling technique for measuring the mitochondrial volume density of *in situ* phrenic motor neurons.
- Mitochondrial volume densities estimated by our MitoTracker Red intrathecal application technique closely approximated those using “gold standard” serial blockface electron microscopy methods.

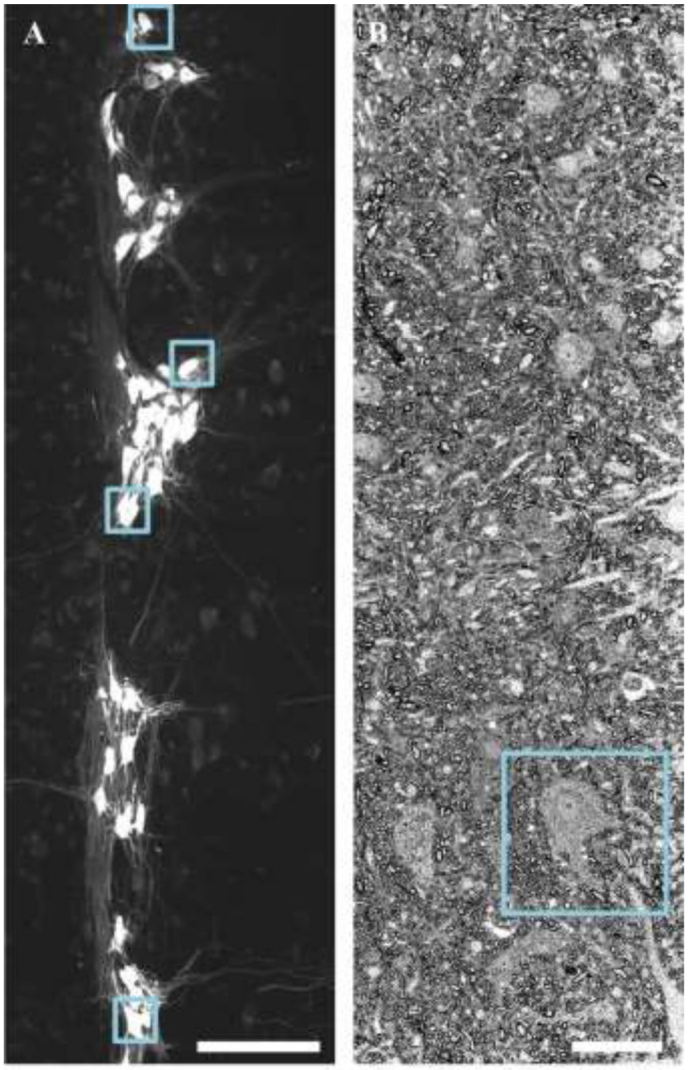

Figure 1: Identification and sampling of motor neurons.

A shows specific labeling of phrenic motor neurons via retrograde labeling with Alexa 488-conjugated CTB is readily apparent in *z*-projection images of horizontal sections (100 μm thick) of cervical (~C_4-C_5 pictured) spinal cord. The blue squares show every 20th phrenic motor neuron, which was then assessed for mitochondrial volume density. **B** shows a survey section (~10 μm thick) containing a putative phrenic motor neuron (inside blue square). These putative phrenic motor neurons later underwent serial block face EM. Scale Bars: A=200 μm; B=20 μm.

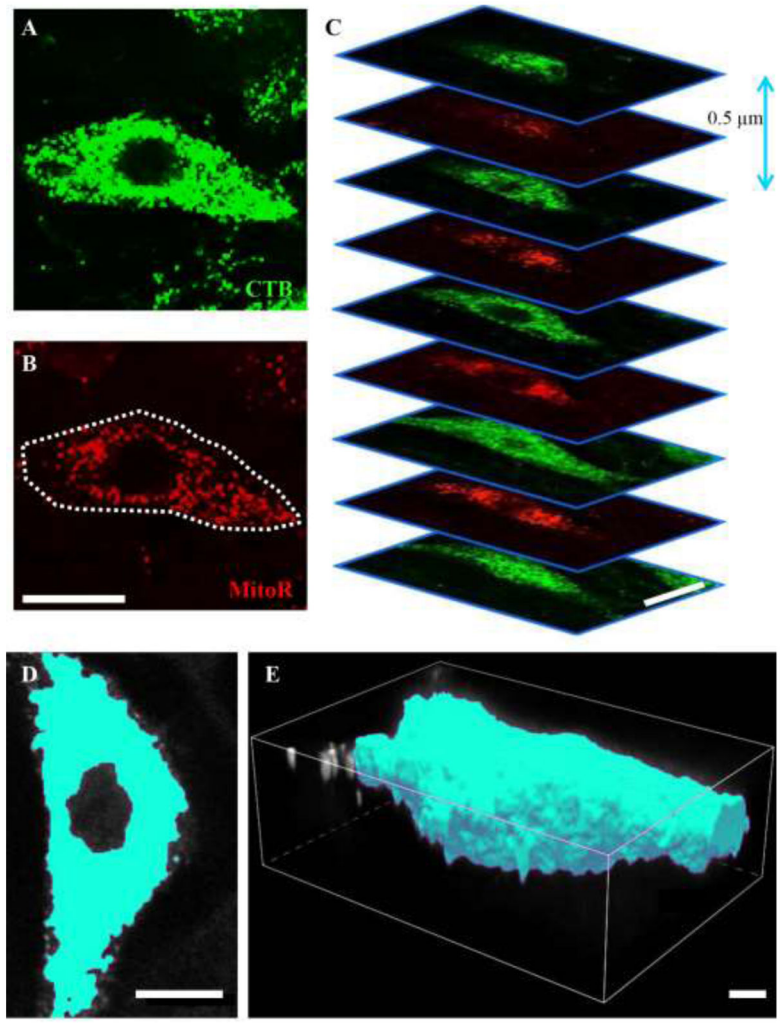

Figure 2: Confocal imaging.

A and **B** show an individual *z*-slice of CTB and MitoTracker red (MitoR) fluorescence, respectively. **C** shows the sequential imaging of CTB labeled phrenic motor neurons and the MitoTracker red signal, with a *z*-step of 0.5 µm. Cyan pseudo-colored examples of the binarisation (D) and surface creation (E) of an individual phrenic motor neuron soma are illustrated. Scale Bars: A=10 µm, B=10 µm, C=5 µm, D=8 µm, E=3 µm.

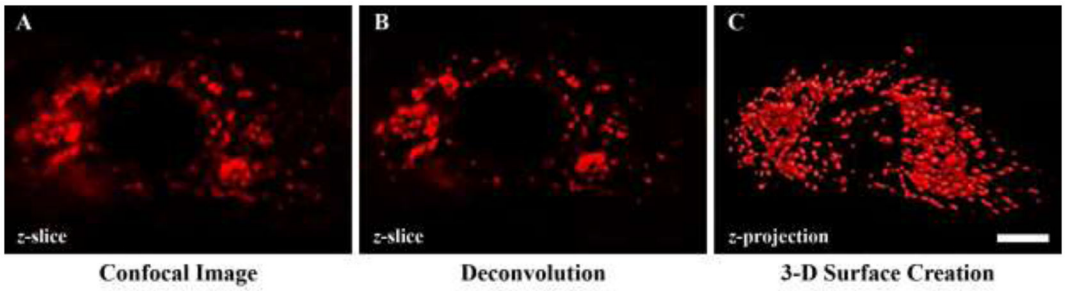

Figure 3: Channel processing of MitoTracker Red.

A Unprocessed MitoTracker Red signal is readily observed at different depths in the *z*-slice within a phrenic motor neuron. **B** Deconvolved MitoTracker Red signal, based on the blind deconvolution (inverse of the idealised point spread function) was done on each *z*-slice within the confocal *z*-stack in the *xy* plane. **C** mitochondrial volume creation based on the local contrast of each deconvolved MitoTracker Red *z*-slice image. These volumes were created using the volume-generating algorithm within the NIS Elements software package. Scale Bar: 3 μm.

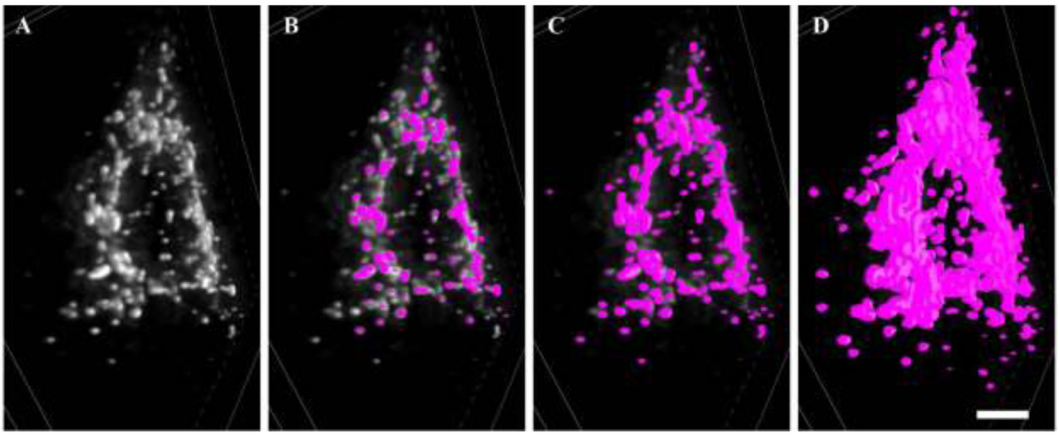

Figure 4: Thresholding of MitoTracker Red.

A shows a 3D *z*-projection of deconvolved MitoTracker Red signal within a phrenic motor neuron. **B** Under-thresholding of deconvolved MitoTracker Red signal, with an abundance of signal uncaptured by the binarisation (fuchsia). **C** shows an acceptable thresholding of deconvolved MitoTracker Red signal, with an abundance of discrete elements and no intense fluorescence outside the binarised volumes. **D** shows an overly inclusive thresholding of deconvolved MitoTracker Red signal, where excessive enlargement of volumes and many superfused elements becoming indistinguishable from one another. Scale Bar: 3 μm.

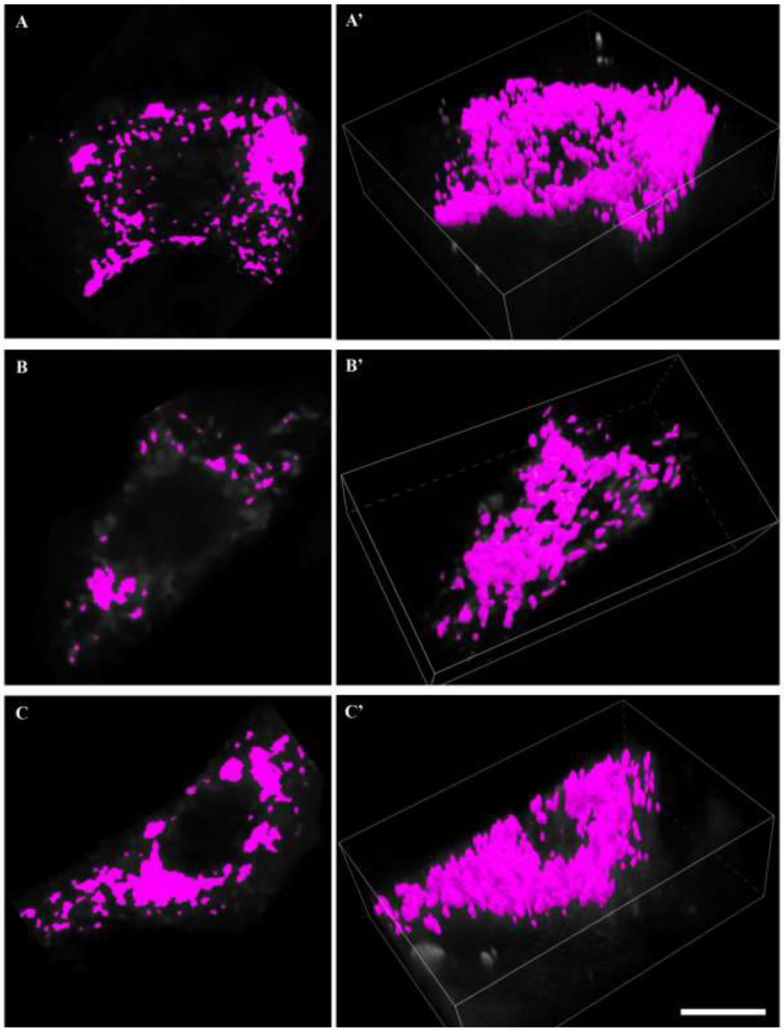

Figure 5: Mitochondrial volume reconstructions.

A, **B** and **C** show binarisation of deconvolved MitoTracker red signal within a mid-nuclear section of a labelled phrenic motor neuron soma. **A'**, **B'** and **C'** show respective mitochondrial volume reconstructions in 3D of the all mitochondrial elements within the labeled phrenic motor neuron. Scale Bar: 10 μm.

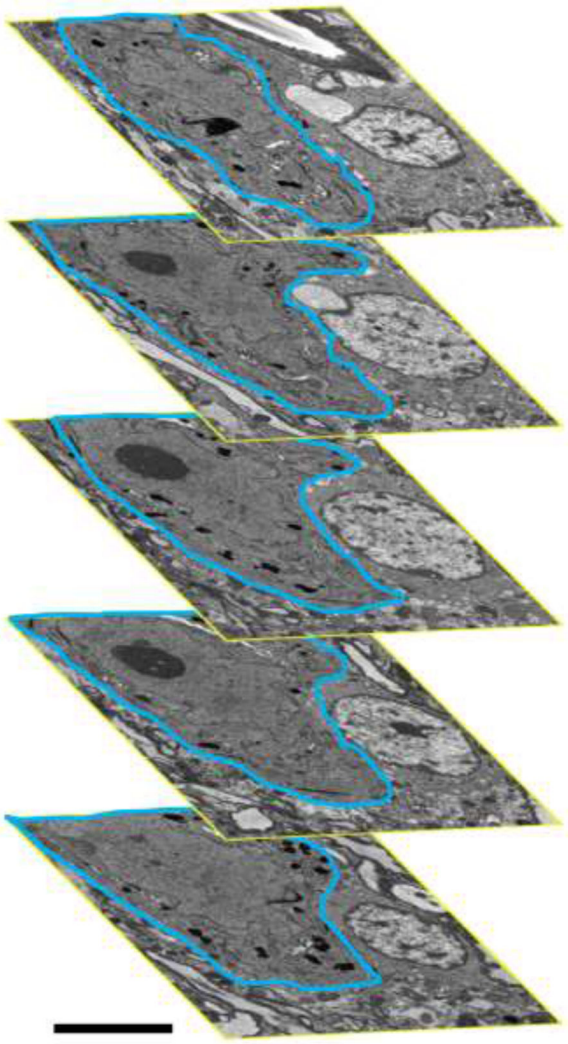

Figure 6: Serial blockface EM.

Serial blockface EM *z*-stacks (containing ~80-250 *z*-slices per motor neuron; in this example 162 slices) were assessed using the Cavalieri sampling technique. Within the bounds of the putative phrenic motor neuron (blue outline) mitochondrial areas were manually traced, with their area, circularity, perimeters, long- and short-axes recorded. At 2 μm intervals from the center mid-nuclear motor neuron section, this process was repeated in both directions. The mean area density of mitochondria were taken for each Cavalieri *z*-slice, and a mitochondrial volume density calculated based on the number of total slices assessed and the distance between each slice (2 μm). Scale Bars: B=5 μm.

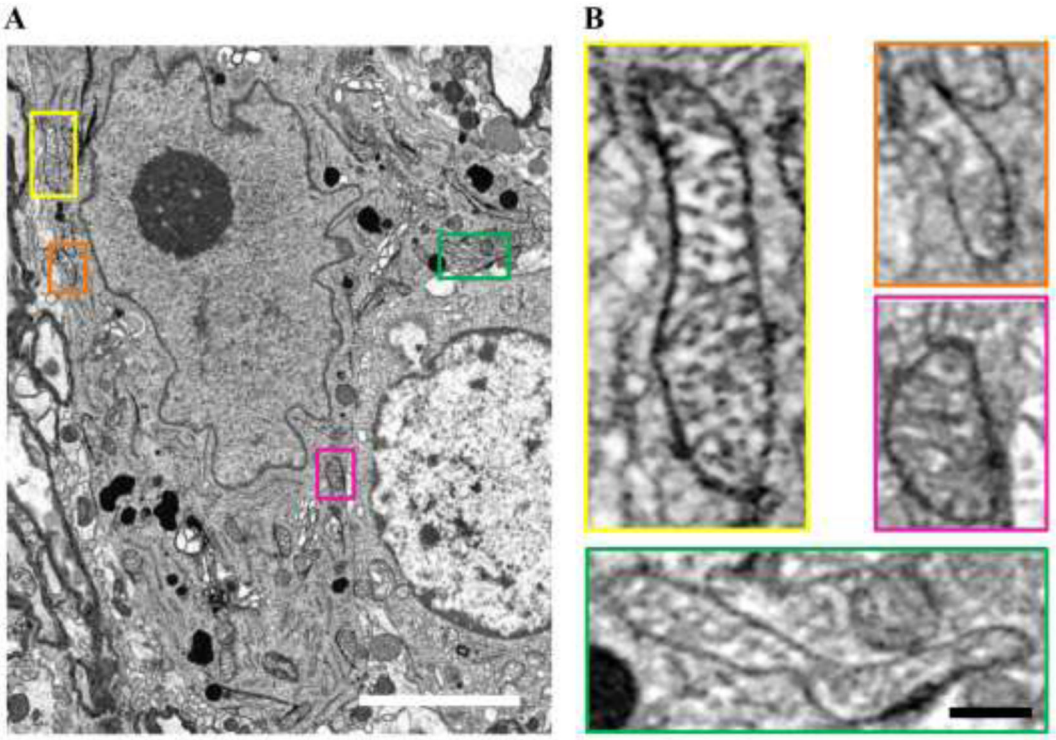

Figure 7: Mitochondria assessment using EM.

A EM blockface image showing a putative phrenic motor neuron, with a prominent nucleolus (dark circle) within the nucleus and a plethora of mitochondria located in perinuclear areas. **B** Insets show higher-magnification images of mitochondria, color coded to location. Note the example of two adjacent mitochondria in the orange inset contrasted with the long filamentous shape mitochondrion in the green inset. It is highly likely in the case of the former that our fluorescent technique does not discriminate between the two individual mitochondria observed in the orange inset. Scale Bars: A=3 μm; Insets=300 nm.

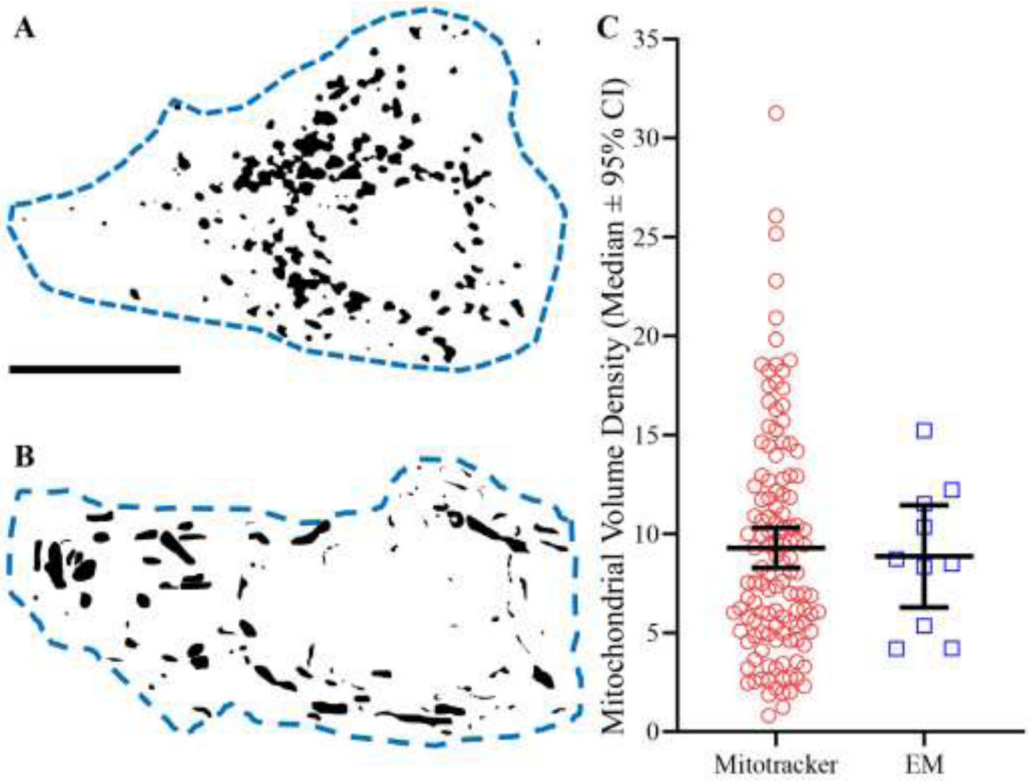

Figure 8: Mitochondrial volume density.

A Silhouette of mitochondrial elements based on deconvolved and binarised MitoTracker Red fluorescence within an identified phrenic motor neuron (dashed blue line). **B** Silhouette of mitochondria traced over serial blockface EM samples within a putative phrenic motor neuron (dashed blue line). C Scatter-plot (median ± 95% CI) showing no difference in mitochondrial volume density estimates between MitoTracker Red (red circles, n=125) and serial blockface EM (blue squares, n=10) techniques (P=0.91; Mann Whitney U-test). Scale Bar: 5 μm.

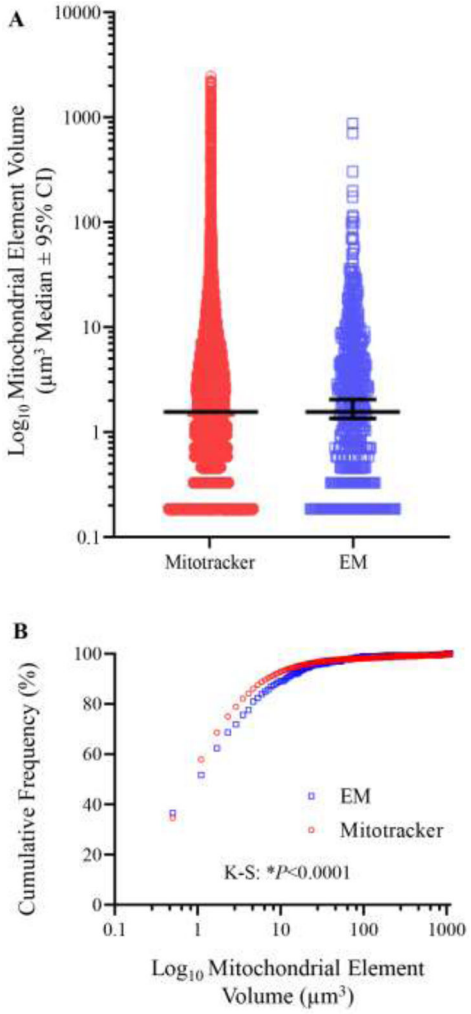

Figure 9: Mitochondrion volumes.

A We observed no difference in the volume estimates of individual mitochondria based on the analysis of either deconvolved MitoTracker Red signal (n=23158) or on Calvalieri volume estimates of serial blockface EM samples (n=1285) are plotted on a Log_{10} scale (P=0.62; Mann Whitney U-test). **B** Cumulative frequency plot showing the propensity of EM analysis to observe smaller individual mitochondrion volumes (P<0.0001, Kolmogorov-smirnov test).

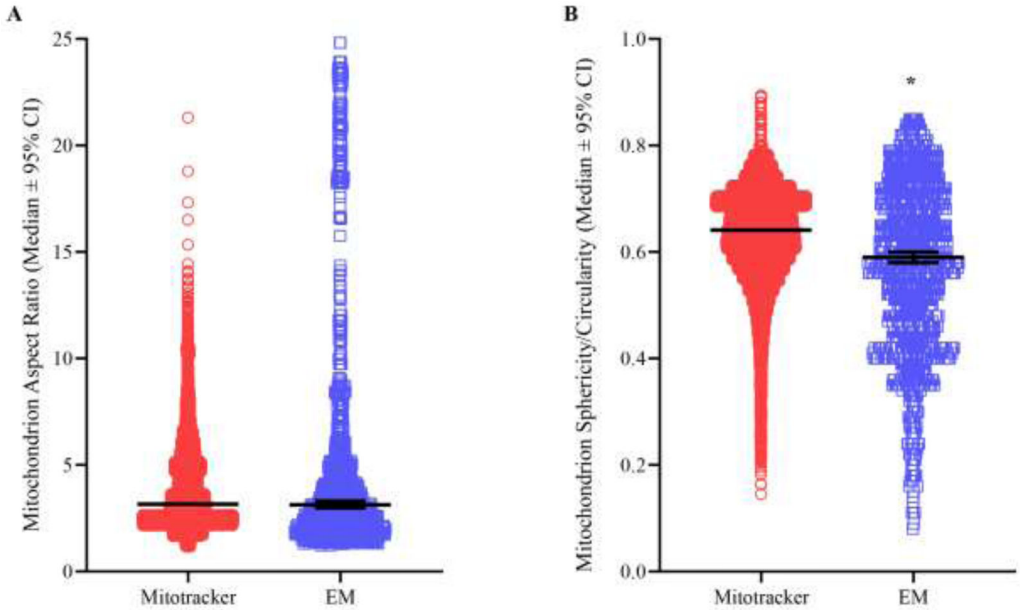

Figure 10: Mitochondrion morphology.

A Scatter-plot (median ± 95% CI) shows no difference in the aspect ratios of individual mitochondrial elements (P=0.13; Mann Whitney U-test) when comparing fluorescent (3.80 ± 0.02, median=3.17, n=23158) to EM techniques (5.96 ± 0.02, median=5.59, n=1285). **B** Scatter plot (median ± 95% CI) shows a significant (P<0.0001; Mann Whitney U-test) yet small magnitude (<8%) reduction in sphericity/circularity of individual mitochondrial elements when assessed with EM techniques (0.58 ± 0.01, median=0.59, n=1285) compared to MitoTracker Red fluorescent (0.63 ± 0.001, median=0.64, n=23158) methods.

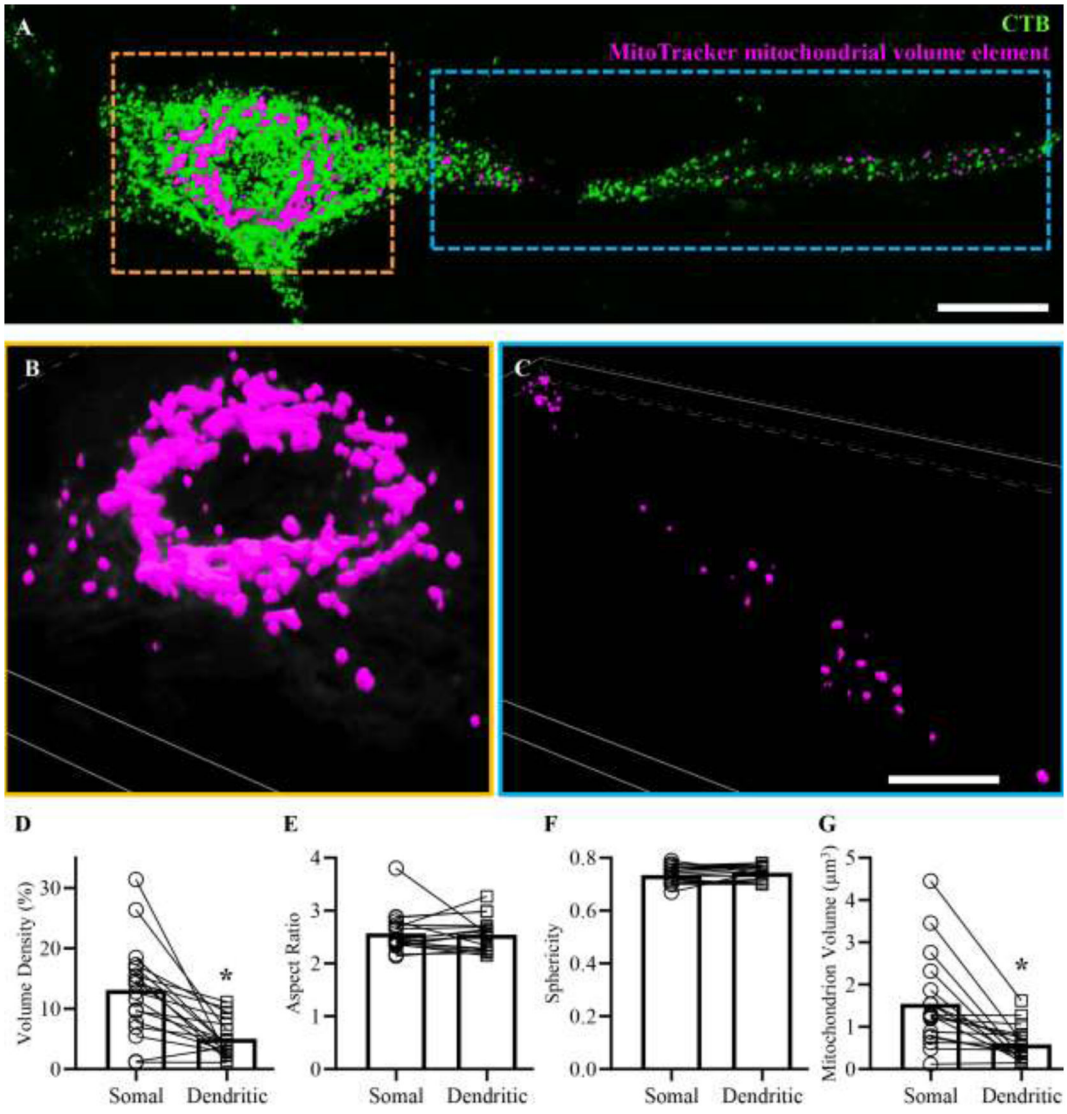

Figure 11: MitoTraker assessment of mitochondrial volumes in somal and dendritic compartments.

A shows a phrenic motor neuron and a portion of the dendritic tree (labelled with CTB, green) superimposed with mitochondrial volume elements (fuchsia). These mitochondrial volume elements were created from 3D reconstructions of deconvolved MitoTracker signal within a somal (**B**) and dendritic (**C**) region of interest from the same cell. **D** shows reduced mitochondrial volume density within the dendritic compartment compared to the soma (P=0.0004, Student's paired t-test). **E** shows unchanged mitochondrial aspect ratios within the dendritic compartment compared to the soma (P=0.56, Wilcoxon test). **F** shows unchanged mitochondrial sphericity within the dendritic compartment compared to the soma (P=0.17, Student's paired t-test). **G** shows a reduction in the volume of individual mitochondrial elements within the dendritic compartment compared to the soma (P<0.0001, Wilcoxon test.). Scale Bar: A=13 μm, B and C=8 μm.

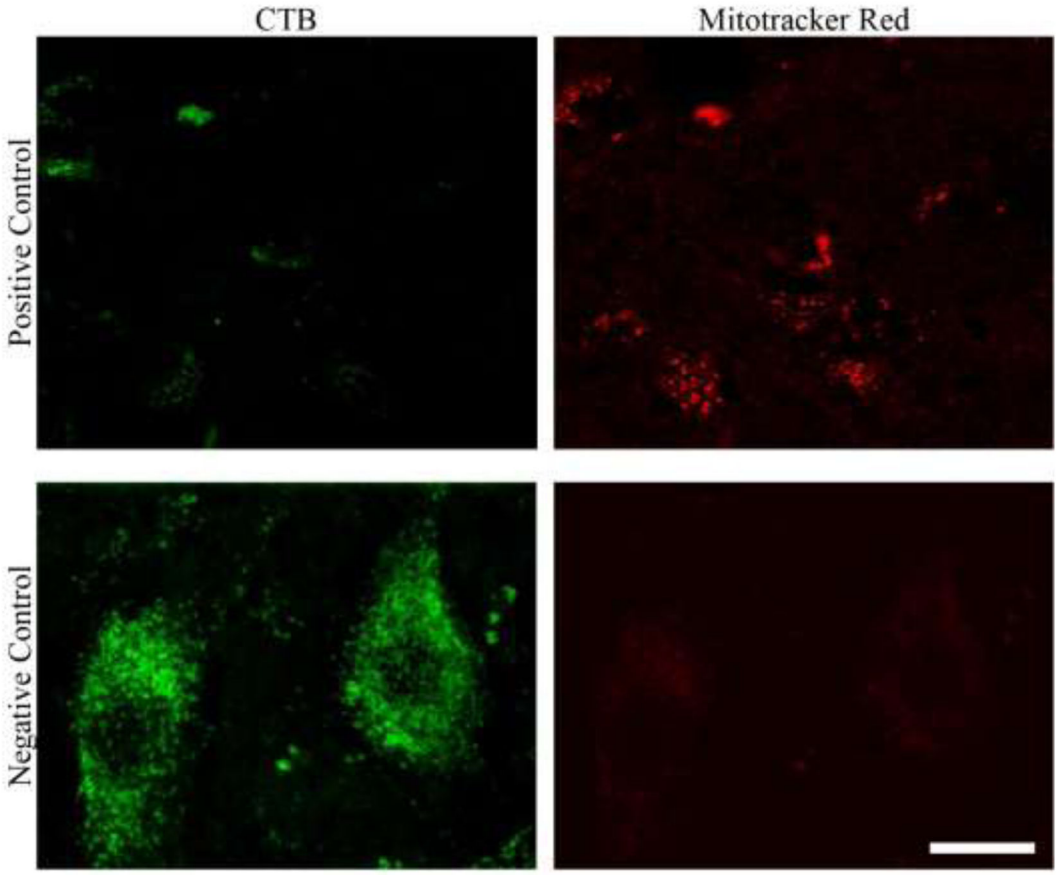

Figure 12: Positive and negative controls.

The top row shows a portion with an absence of labeled phrenic motor neurons (left), albeit with a reliable MitoTracker Red fluorescent signal. The bottom row shows little non-specific fluorescence on the 575-630 nm channel when an Alexa 488-conjugated labeled phrenic motor neuron was imaged without any intrathecal application of MitoTraker Red (i.e., a negative control). Scale Bar: 5 μm.

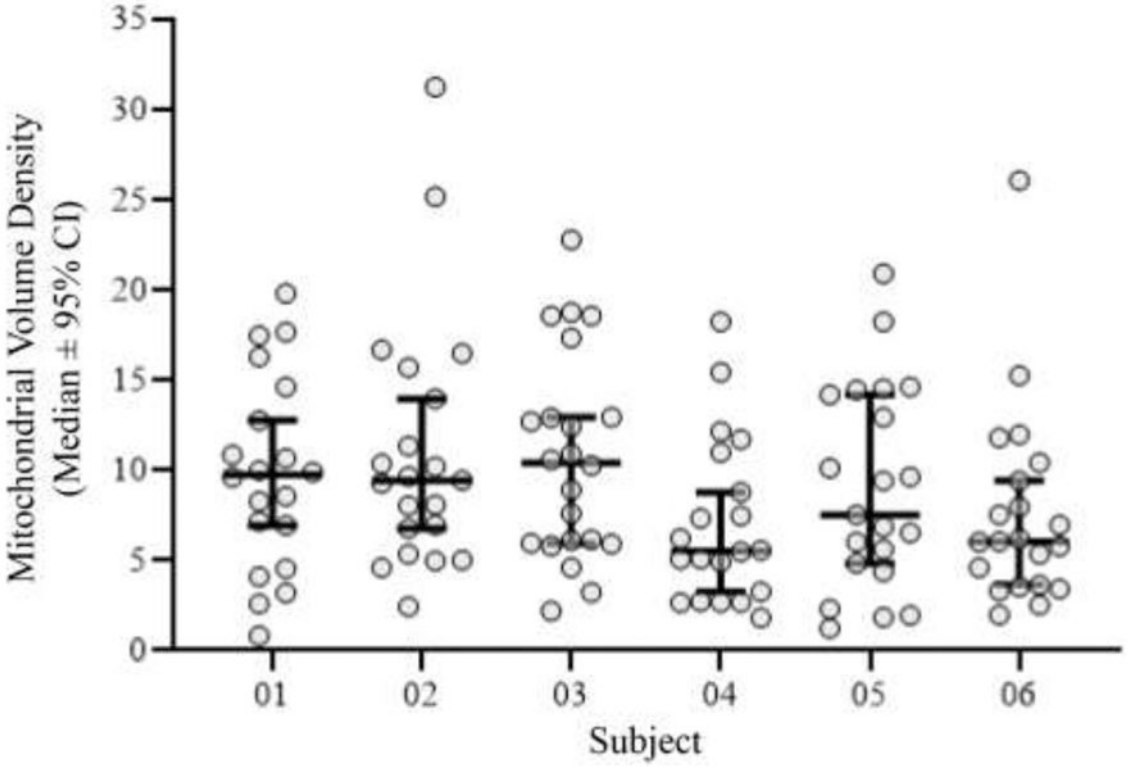

Figure 13: Mitochondrial volume density assessed by MitoTracker Red fluorescence is reliable and repeatable across subjects.

The range of mitochondrial volume densities within labeled phrenic motor neurons in rats was ~1-29%. Scatter-plot (median ± 95% CI) shows that there was no difference in the mean mitochondrial volume density for phrenic motor neurons when compared between rats, with mean values ranging from ~7.5-11% and medians ranging from ~6-10% volume density (P=0.18; Kruskal-Wallis test).

Table 1:

Phrenic motor neuron mitochondrial density and morphology is not different between sexes.

Parameter	Females (*n*)	Males (*n*)	P-Value
Somal Mitochondrial Volume Density (%)	8.95 ± 0.38 (*63*)	9.47 ± 0.55 (*62*)	*P*=0.73[a]
Somal Mitochondrial Aspect Ratio	3.73 ± 0.21 (*63*)	3.65 ± 0.18 (*62*)	*P*=0.90[a]
Somal Mitochondrial Sphericity	0.67 ± 0.01 (*63*)	0.68 ± 0.01 (*62*)	*P*=0.33[a]
Dendritic Mitochondrial Volume Density (%)	4.82 ± 2.36 (*9*)	5.33 ± 2.53 (*9*)	*P*=0.79[b]

All data presented as mean ± 95% CI.

[a]Mann-Whitney *u*-test.

[b]Student's paired *t*-test. The *n* referred to in the table is either motor neurons or dendrites.